공학박사학위논문

3차원 자동차 모델의 항력 감소에 관한 실험적 연구: 수동적 및 능동적 유동제어

An experimental study on the drag reduction on a three-dimensional model vehicle: passive and active flow controls

2020 년 2 월

서울대학교 대학원

기계항공공학부

김 동 리

3차원 자동차 모델의 항력 감소에 관한 실험적 연구: 수동적 및 능동적 유동제어

An experimental study on the drag reduction on a three-dimensional model vehicle: passive and active flow controls

지도교수 최 해 천

이 논문을 공학박사 학위논문으로 제출함

2019년 10월

서울대학교 대학원

기계항공공공학부

김 동 리

김동리의 공학박사 학위 논문을 인준함

2019년 12월

위 원 장: 박 형 민

부위원장: 최 해 천

위 원: 도 형 록

위 원: 황 원 태

위 원: 이 정 일

An experimental study on the drag reduction on a three-dimensional model vehicle: passive and active flow controls

Dongri Kim
Department of Mechanical & Aerospace Engineering
Seoul National University

Abstract

Reducing the aerodynamic drag on a road vehicle has always been an important issue both in academia and industries. Therefore, many of studies on the drag reduction on a model vehicle have been conducted so far both by passive and active means. Although the flow control devices considered in the previous studies have shown remarkable performances, they have also possessed some limitations that cannot be overlooked. The passive devices inevitably require fixed appendages or even a shape modification of the vehicle model and may not perform well at various vehicle speeds. On the other hand, the active devices which mainly utilize blowing/suction devices may not be easily applicable in practice because they often require an external fluid source/sink and even a rather complicated apparatus for driving them. Therefore, in this dissertation, automatic moving deflector and dielectric barrier discharge (DBD) plasma actuator are suggested as alternative passive and active flow control devices in part I and part II, respectively.

In part I, we introduce a bio-mimetic device for the reduction of the

drag force on a three-dimensional model vehicle, the Ahmed body (Ahmed *et al.* 1984). The device, called AMD (automatic moving deflector), is designed inspired by the movement of secondary feathers on bird's wing suction surface: i.e., secondary feathers pop up when massive separation occurs on bird's wing suction surface at high angles of attack, which increases the lift force at landing. The AMD is applied to the rear slanted surface of the Ahmed body to control the flow separation there. The angle of the slanted surface considered is 25° at which the drag coefficient on the Ahmed body is highest. The wind tunnel experiment is conducted at $Re_H = 1.0 \times 10^5 - 3.8 \times 10^5$, based on the height of the Ahmed body (H) and the free-stream velocity (U_∞). Several AMDs of different sizes and materials are tested by measuring the drag force on the Ahmed body, and showed drag reductions up to 19%. The velocity and surface-pressure measurements show that AMD starts to pop up when the pressure in the thin gap between the slanted surface and AMD is much larger than that on the upper surface of AMD. We also derive an empirical formula that predicts the critical free-stream velocity at which AMD starts to operate. Finally, it is shown that the drag reduction by AMD is mainly attributed to a pressure recovery on the slanted surface by delaying the flow separation and suppressing the strength of the longitudinal vortices emanating from the lateral edges of the slanted surface.

In part II, we apply a wire-to-plate and sawtooth DBD plasma actuators to the Ahmed body for drag reduction at the free-stream velocities of $U_\infty = 10 - 20$ m/s. For the case of the wire-to-plate actuator, an actuator whose exposed electrode is made of a thin wire of 11 μm diameter is located at the front edge of the slanted surface of the Ahmed body, and its spanwise length and applied voltage are varied. The induced mean veloc-

ity by the actuator reaches up to about 4.2 m/s at the applied voltage of 9 kV_{p-p}. With actuation, the drag is reduced by the amount of maximum 10% at $U_\infty = 10$ m/s, and the efficiency is up to $0.1 - 0.12$ depending on the spanwise length of the actuator, applied voltage, and free-stream velocity. The drag reduction and efficiency of the present wire-to-plate actuator are higher than those of a conventional plate-to-plate actuator. With surface-pressure and PIV measurements, it is shown that the flow above the slanted surface is significantly affected by the spanwise length of the actuator, and the streamwise momentum induced by the actuator suppresses the flow separation at the front edge of the slanted surface and recovers the pressure on the slanted and vertical base surfaces, resulting in drag reduction. Moreover, it is found that the drag reduction rate and efficiency at higher U_∞ of 20 m/s can be further enhanced up to 8.2% and 0.56, respectively, by employing a sawtooth-shaped exposed electrode, whereas those of the linear wire-to-plate actuator are up to 2.7% and 0.1, respectively, at the same U_∞. With the plasma actuator with a sawtooth-shaped exposed electrode, the development of the shear layer over the slanted surface is significantly accelerated, enhancing the mixing inside the boundary layer. As a result, the momentum induced by the actuator is effectively supplied into the separated boundary layer, leading to a significant suppression of the flow separation at the front edge of the slanted surface, despite of high U_∞.

Finally, in part III, we summarize the effect of the passive (AMD) and active (wire-to-plate plasma actuator) flow control devices and propose a comparative analysis of their mechanisms responsible for the drag reduction. Both devices suppress the formation of the secondary separation bubble on the slanted surface, leading to a significant pressure recovery

there. On the other hand, by each device, the size, strength and location of the main separation bubbles are substantially different, for which the pressure change on the vertical base surface appears differently for each device. AMD suppresses the strength of the longitudinal vortices whereas the plasma actuator has little effect on them. Consequently, the pressure recovery on the slanted surface solely contributes to the drag reduction for the case of AMD, while the pressure recoveries on the slanted and vertical base surfaces both contribute to the drag reduction for the case of the plasma actuator.

Keywords: model vehicle, flow separation, passive flow control, active flow control, pressure recovery, drag reduction

Student number: 2013-23829

Contents

Abstract i

Contents v

List of Figures viii

Nomenclature xv

Part I Drag reduction on a three-dimensional model vehicle by a passive flow control 1

1 Introduction 2

2 Control device and experimental setup 7

2.1. Model vehicle and control device 7

2.2. Experimental setup and measurement systems 9

3 Results and discussion 17

3.1. Drag variation 17

3.2. Operating mechanism of AMD 19

3.3. Drag-reduction mechanism 22

4 Conclusions 33

Part II Drag reduction on a three-dimensional model

vehicle by an active flow control **35**

1 Introduction **36**

2 Experimental details **43**

2.1. Model vehicle 43

2.2. DBD plasma actuator and power supply system 43

2.3. Experimental setup and measurement system 44

3 Results **52**

3.1. Characteristics of the plasma actuator 52

3.2. Drag variation 53

4 Discussions **59**

4.1. Flow modifications for the case of largest drag reduction rate 59

4.2. Effect of the actuator length on the flow field 60

5 Further drag reduction at high Re_H employing a sawtooth-shaped electrode **65**

5.1. Characteristics of the sawtooth plasma actuator 66

5.2. Drag variation 67

5.3. Flow modifications 68

6 Conclusions **78**

Part III Drag reduction mechanisms by passive and active flow controls: comparison and analysis **81**

1 Comparative analysis of the drag reduction mechanisms by the passive and active flow control devices **82**

References **86**

List of Figures

Part I Drag reduction on a three-dimensional model vehicle by a passive flow control

1.1 Skua wing in landing approach (photograph courtesy of Ingo Rechenberg). 6

2.1 Ahmed body (redrawn from Ahmed *et al.* 1984). 12

2.2 Variation of the drag coefficient of the Ahmed body with the slant angle at $Re_H = 1.15 \times 10^6$ (Ahmed *et al.* 1984, from Choi *et al.* 2014). 13

2.3 AMD attached on the Ahmed body and its geometric configuration. 14

2.4 Schematic diagram of the experimental setup for the drag and surface-pressure measurements. 15

2.5 Schematic diagram of the experimental setup for the PIV measurement. 16

3.1 Variation of the drag coefficient with the slant angle. . . . 24

3.2 Variations of the drag reduction rate with the length of AMDs made of (a) transparent acrylic and (b) hard strawboard. 25

3.3 Contours of the mean pressure coefficient on the AMD surfaces ($Re_H = 1.0 \times 10^5$): (a) lower surface; (b) upper surface; (c) their difference. Note that the pressures are measured on the slanted surface of the Ahmed body and converted to those on the AMD surfaces. White circles in this figure denote the locations of the pressure measurement. 26

3.4 Contours of the instantaneous streamwise velocity at the centre plane ($z/H = 0$) (upper) and the contours of the instantaneous streamwise vorticity together with the instantaneous velocity vectors on a cross-flow plane ($x/H = -0.10$) (lower) ($Re_H = 1.2 \times 10^5$). Here, (a – c) and (d – f) show the time sequence: before, during, and after the pop-up (left to right). The locations of AMD are shown in black lines. 27

3.5 Contours of the mean streamwise velocity and the mean streamlines at (x, y) planes without (a, c, e) and with AMD (b, d, f). $Re_H = 2.9 \times 10^5$. 28

3.6 Contours of the mean pressure coefficient on the left halves of the slanted (upper) and vertical base (lower) surfaces ($Re_H = 2.9 \times 10^5$): (a) without AMD; (b) with AMD. White circles in this figure denote the locations of the pressure measurement. 29

3.7 Secondary flows in the wake: contours of the mean streamwise vorticity and the mean velocity vectors on the cross-flow planes without (upper) and with AMD (lower). (a) $x/H = 0.25$; (b) 0.50; (c) 0.75; (d) 1.0; (e) 1.5. 30

3.8 Contours of the Reynolds stresses on the (x, y) plane at $z/H = 0$ without (a, c, e) and with AMD (b, d, f). (a, b) $\overline{u'u'}/U_\infty^2$; (c, d) $\overline{v'v'}/U_\infty^2$; (e, f) $-\overline{u'v'}/U_\infty^2$. 31
3.9 Contours of the Reynolds stresses on the cross-flow plane at $x/H = 0.75$ without (upper) and with AMD (lower). (a) $\overline{w'w'}/U_\infty^2$; (b) $\overline{v'v'}/U_\infty^2$; (c) $-\overline{w'v'}/U_\infty^2$. 32

Part II Drag reduction on a three-dimensional model vehicle by an active flow control

1.1 Schematic diagram of a typical DBD plasma actuator. . . 42

2.1 Schematic diagram of the Ahmed body (redrawn from Ahmed *et al.* 1984). 48
2.2 Wire-to-plate plasma actuator attached on the Ahmed body. Here l is the actuator length. 49
2.3 Schematic diagram of the experimental setup for the drag, surface-pressure and voltage measurements. 50
2.4 Planes of interest for the PIV measurement. 51

3.1 Variations of the mean velocity induced by the wire-to-plate and plate-to-plate plasma actuators with the applied voltage (measured at 5 mm downstream from the wire electrode and 1 mm above the dielectric layer). 55
3.2 Variations of the mean dissipated power per unit length of the wire-to-plate and plate-to-plate plasma actuators with the applied voltage. 56

3.3 Variations of the drag reduction rate (ΔD) with the applied voltage and actuator length by the wire-to-plate (solid lines with solid symbols) and plate-to-plate (dotted lines with open symbols) actuators: (a) $Re_H = 0.96 \times 10^5$; (b) 1.44×10^5; (c) 1.92×10^5. 57

3.4 Variations of the control efficiency with the applied voltage and actuator length by the wire-to-plate (solid lines with solid symbols) and plate-to-plate (dotted lines with open symbols) actuators: (a) $Re_H = 0.96 \times 10^5$; (b) 1.44×10^5; (c) 1.92×10^5. 58

4.1 Mean streamlines and contours of the mean streamwise velocity ($Re_H = 0.96 \times 10^5$): (a, b) without and (c, d) with the actuation ($l/Z = 0.8$ and $V_{\mathrm{a}} = 9$ $\mathrm{kV_{p-p}}$). The purple areas at the front edge of the slanted surface in (c) and (d) could not be measured due to the light emission from the plasma actuator. 62

4.2 Contours of the mean pressure coefficient on the slanted and vertical base surfaces ($Re_H = 0.96 \times 10^5$): (a) without actuator; (b) with the actuator of $l/Z = 0.5$; (c) $l/Z = 0.8$; (d) $l/Z = 1.0$ ($V_{\mathrm{a}} = 9$ $\mathrm{kV_{p-p}}$). White circles in this figure denote the locations of the pressure measurement. . 63

4.3 Mean streamlines and contours of the Reynolds shear stress ($-\overline{u'v'}$) ($Re_H = 0.96 \times 10^5$): (a) without actuator; (b) with the actuator of $l/Z = 0.5$; (c) $l/Z = 0.8$ ($V_{\mathrm{a}} = 9$ $\mathrm{kV_{p-p}}$). The purple areas at the front edge of the slanted surface in (b) and (c) could not be measured due to the light emission from the plasma actuator. 64

5.1 Sawtooth plasma actuator attached on the Ahmed body and the geometric configurations of its exposed electrode. 70

5.2 Variations of the mean velocity induced by the sawtooth plasma actuators of $\lambda/h = 1.2$ and 2 with the applied voltage and spanwise location (measured at 5 mm downstream from the wire electrode and 1 mm above the dielectric layer). Here, the solid and dotted horizontal lines denote the induced velocities by the wire-to-plate and plate-to-plate actuators, respectively (from figure 3.1), and $z = 0$ is where a root is. 71

5.3 Variations of the mean dissipated power of the sawtooth and linear plasma actuators with the applied voltage ($l/Z = 0.8$). 72

5.4 Variations of the drag reduction rate (ΔD) with the applied voltage by the sawtooth and linear actuators: (a) $Re_H = 0.96 \times 10^5$; (b) 1.44×10^5; (c) 1.92×10^5 ($l/Z = 0.8$). 73

5.5 Variations of the control efficiency with the applied voltage by the sawtooth and linear actuators: (a) $Re_H = 0.96 \times 10^5$; (b) 1.44×10^5; (c) 1.92×10^5 ($l/Z = 0.8$). 74

5.6 Mean streamlines and contours of the mean streamwise velocity ($Re_H = 1.92 \times 10^5$): (a) without and (b) with the actuation by the wire-to-plate actuator and (c, d) sawtooth actuator of $\lambda/h = 1.2$ at the root- and tip-planes, respectively ($l/Z = 0.8$ and $V_\mathrm{a} = 9$ $\mathrm{kV_{p-p}}$). Here, (a – c) and (d) are measured at $z/Z = 0$ and -0.02, respectively. The purple areas at the front edge of the slanted surface in (b – d) could not be measured due to the light emission from the plasma actuator. 75

5.7 Contours of the mean pressure coefficient on the slanted and vertical base surfaces ($Re_H = 1.92 \times 10^5$): (a) without and (b) with the actuation by the wire-to-plate actuator and (c) sawtooth actuator of $\lambda/h = 1.2$ ($l/Z = 0.8$ and $V_\mathrm{a} = 9$ $\mathrm{kV_{p-p}}$). White circles in this figure denote the locations of the pressure measurement. 76

5.8 Mean streamlines and contours of the Reynolds shear stress ($-\overline{u'v'}$) ($Re_H = 1.92 \times 10^5$): (a) without and (b) with the actuation by the wire-to-plate actuator and (c, d) sawtooth actuator of $\lambda/h = 1.2$ at the root- and tip-planes, respectively ($l/Z = 0.8$ and $V_\mathrm{a} = 9$ $\mathrm{kV_{p-p}}$). Here, the spatial resolution is $0.00463H$, and (a – c) and (d) are measured at $z/Z = 0$ and -0.02, respectively. The purple areas at the front edge of the slanted surface in (b – d) could not be measured due to the light emission from the plasma actuator. 77

Part III Drag reduction mechanisms by passive and ac-

tive flow controls: comparison and analysis

1.1 I. Contours of the mean streamwise velocity and the mean streamlines at (x, y) center plane and contours of the mean streamwise vorticity and the mean velocity vectors on the cross-flow plane at $x/H = 0.25$ (a, c) without and (b, d) with AMD. $Re_H = 2.9 \times 10^5$ (from figures 3.5 and 3.7 in part I). II. Contours of the mean streamwise velocity and the mean streamlines at (x, y) center plane (from figure 4.1 in part II) and contours of the mean streamwise vorticity and the mean velocity vectors on the cross-flow plane at $x/H = -0.25$ (e, g) without and (f, h) with the wire-to-plate plasma actuator. $Re_H = 0.96 \times 10^5$. 84

1.2 I. Contours of the mean pressure coefficient on the left halves of the slanted (upper) and vertical base (lower) surfaces (a, b) without and (c, d) with AMD. $Re_H = 2.9 \times 10^5$ (from figure 3.6 in part I). II. Contours of the mean pressure coefficient on the left halves of the slanted (upper) and vertical base (lower) surfaces (e, f) without and (g, h) with the wire-to-plate plasma actuator. $Re_H = 0.96 \times 10^5$ (from figure 4.2 in part II). 85

Nomenclature

Roman symbols

A_{f}	Frontal area of the model
C_{m}	Capacitance of the monitor capacitor
C_D	Drag coefficient
C_P	Pressure coefficient
$C_{P\mathrm{l}}$	Pressure coefficient on the lower side of AMD
$C_{P\mathrm{u}}$	Pressure coefficient on the upper side of AMD
D	Time-averaged drag
D_{AMD}	Drag on the model with AMD
D_{base}	Drag on the model without plasma actuation
D_{control}	Drag on the model with the plasma actuation
D_{NO}	Drag on the model without AMD
E	Young's modulus
f	Driving frequency
G	Ground clearance
H	Model height
h	Tooth height
I	Second moment of area
l	Longitudinal length of AMD (part I);
	Actuator length (part II)
P	Time-averaged surface-pressure
P_∞	Static pressure at the free-stream
$P_{\mathrm{D}_{\mathrm{linear}}}$	Dissipated power of the linear plasma actuator

$P_{\mathrm{D}_{\mathrm{sawtooth}}}$	Dissipated power of the sawtooth plasma actuator
P_{D}	Dissipated power
P_{d}	Dissipated power per unit actuator length
Re_H	Reynolds number, $Re_H = U_\infty H/\nu$
S	Length of the slanted surface
s	Coordinate along the length of the slanted surface originated at its rear edge
t	Thickness of AMD
T_{AMD}	Torque exerted by AMD weight
T_P	Torque exerted by the pressure difference
U	Mean streamwise velocity
u	Streamwise velocity
U_∞	Free-stream velocity
$\overline{u'u'}, \overline{v'v'}, \overline{w'w'}$	Reynolds normal stresses
$-\overline{u'v'}, -\overline{w'v'}$	Reynolds shear stresses
V_{a}	Applied voltage
V_{m}	Voltage across the monitor capacitor
x, y, z	Cartesian coordinates originated at the spanwise center of the bottom of the vertical base surface
x', y'	Cartesian coordinates originated at the leading edge of the raised floor
Z	Model width

Greek symbols

α	Slant angle
ΔD	Drag reduction rate
δ^*	Displacement thickness

δ_{99}	Boundary layer thickness
η	Control efficiency
λ	Tooth width
ν	Kinematic viscosity
Ω_x	Mean streawise vorticity
ω_x	Streawise vorticity
ρ	Air density
ρ_{AMD}	Mass per unit area of AMD
θ	Deflection angle of AMD
ξ	Coordinate along the longitudinal length of AMD originated at its leading edge

Abbreviations

AC	Alternating current
AMD	Automatic moving deflector
DBD	Dielectric barrier discharge
HWA	Hot-wire anemometry
PIV	Particle image velocimetry
PSVG	Plasma streamwise vortex generator

Part I.

Drag reduction on a three-dimensional model vehicle by a passive flow control

This part is based on "Kim, D., Lee, H., Yi, W. & Choi, H. 2016 A bio-inspired device for drag reduction on a three-dimensional model vehicle. *Bioinspiration & Biomimetics* **11**, 026004".

Chapter 1

Introduction

The rapid increase in fuel prices and the depletion of petroleum resources have unceasingly raised the need to reduce fuel consumption of road vehicles. In an effort to minimize fuel consumption, automobile industries have regarded the gas mileage improvement of road vehicles as a core research subject. Furthermore, a world-wide regulation of greenhouse gas emissions in recent years has made it more urgent to develop technologies to reduce fuel consumption. Reducing the aerodynamic drag has been an effective strategy for reducing the fuel consumption of road vehicles. Hucho & Sovran (1993) suggested that the aerodynamic drag makes up 46% of fuel consumption for a midsize car in highway driving. Moreover, McCallen *et al.* (1999) reported that a typical modern tractor-trailer possessing the drag coefficient of 0.6 takes 65% of the total fuel expenditure from overcoming the aerodynamic drag. They suggested that reducing the drag coefficient from 0.6 to 0.3 for a typical tractor-trailer would result in a 43% fuel savings. Because classical drag reduction strategies like shape optimization of road vehicles have been widely used since 1970s, the vehicle shapes nowadays may not be so easy to modify. Therefore, new strategies to achieve further drag reduction have to be developed.

Many active and passive flow control devices for aerodynamic drag reduction of road vehicles have been actively developed so far (see, for a review, Choi *et al.* (2014)). The active control is being widely investigated

mainly with a blowing/suction device. For example, Joseph *et al.* (2012) and Gilliéron & Kourta (2013) obtained about 8% and 20% drag reductions, respectively, by periodic forcing with pulsed jets installed around the front edge of the slanted surface of the Ahmed body. Rouméas *et al.* (2009) applied continuous suction on the upper part of the slanted surface to suppress the separation bubble there and obtained about 17% drag reduction. Other than a blowing/suction device, Aider *et al.* (2010) used an array of trapezoidal vortex generators that were actively controlled on the roof of a modified Ahmed body with a curved rear part and obtained up to 14% drag reduction. Meanwhile, passive control devices using vortex generators or flaps have been also developed. For example, Pujals *et al.* (2010) attached an array of cylindrical vortex generators on the rear roof of the Ahmed body at the slant angle of 25° and acquired about 10% drag reduction. Beaudoin & Aider (2008) applied flaps to the edges of the rear part of a modified Ahmed body at the slant angle of 30° and obtained up to 25% drag reduction. Fourrié *et al.* (2011) also used a flap attached to the front edge of the slanted surface with various deflection angles and obtained drag reductions up to 9%.

Although successful results have been reported as mentioned above, some unfavourable properties lie in the previous control devices. The active control methods inevitably demand external power to operate and are inherently more difficult to install than the passive ones. On the other hand, the passive control methods require fixed appendages on the model and may not perform well at various vehicle speeds. Therefore, some alternative devices for flow control that do not possess those unfavourable aspects should be developed.

One of the promising areas in this direction is the bio-mimetic ap-

proach (or bio-inspired approach) in which solutions to engineering problems are obtained from some morphological features of living creatures in nature (Choi *et al.* 2012). For example, Mercedes-Benz conceptually designed a bionic car whose exterior shape mimics that of a boxfish; despite its boxy and cube-shaped body, this car has a drag coefficient of 0.19. As compared to generic passenger cars that have typical drag coefficients around 0.3 (Hucho & Sovran 1993), the drag coefficient of this bionic car is surprisingly low.

One interesting bio-mimetic approach is the flow control device inspired by the secondary feathers of a bird's wing. This idea was initially developed by Liebe (1979) who carefully observed the flight of a bird and noticed that the secondary feathers on the wing suction surface pop up while it lands (figure 1.1). Liebe (1979) described that once flow separation starts to develop on a wing, reverse flow occurs inside the separation bubble, and light secondary feathers pop up responding to the reverse flow. Then, the secondary feathers prevent further propagation of flow separation, thereby leading to the delay of flow separation. Although he first pointed it out as a high-lift device of a biological wing, there had been no successful applications of this idea until the study of Bechert *et al.* (1997). They installed a movable deflector, inspired by the secondary feathers of a bird's wing, on two-dimensional aerofoils (HQ17 and HQ41), and investigated the deflector movement and its aerodynamic performance. They also conducted a real flight test by applying movable deflectors on a glider plane and obtained lift enhancement by more than 10%. Furthermore, there have been a few follow-up numerical studies of this work (Schatz *et al.* 2004; Meyer *et al.* 2007). Some researchers even extended its application to other aerofoil models and experimen-

tally tested its performance (Kernstine *et al.* 2008; Schlüter 2010; Wang & Schlüter 2012). This device delayed flow separation at high angles of attack by blocking the reverse flow from the trailing edge to the suction peak region, and produced lift enhancement.

We believe that the concept of this novel bio-mimetic flow control device should be also utilized to the flow over a bluff body, in which the delay of flow separation or weakening of massive flow separation is an important strategy for drag reduction (Beaudoin *et al.* 2006; Choi *et al.* 2006, 2008). Notably, this bio-mimetic device can remove the demerits of the conventional control devices, in that it is a passive device (i.e. no external power is required to operate) but little changes the body shape when it does not operate (see later in this paper). So far, only one study has been made for the application of this device to the flow over a bluff body; Mazellier *et al.* (2012) obtained drag reductions up to 25% by applying this device to a square cylinder, but they did not provide any detailed flow analysis. Therefore, in our study, we apply this bio-mimetic device, called AMD (automatic moving deflector; inspired by the dynamics of the secondary feathers of a bird's wing) hereafter, to a three-dimensional model vehicle for the reduction of the aerodynamic drag, and investigate the mechanism responsible for its operation and drag reduction.

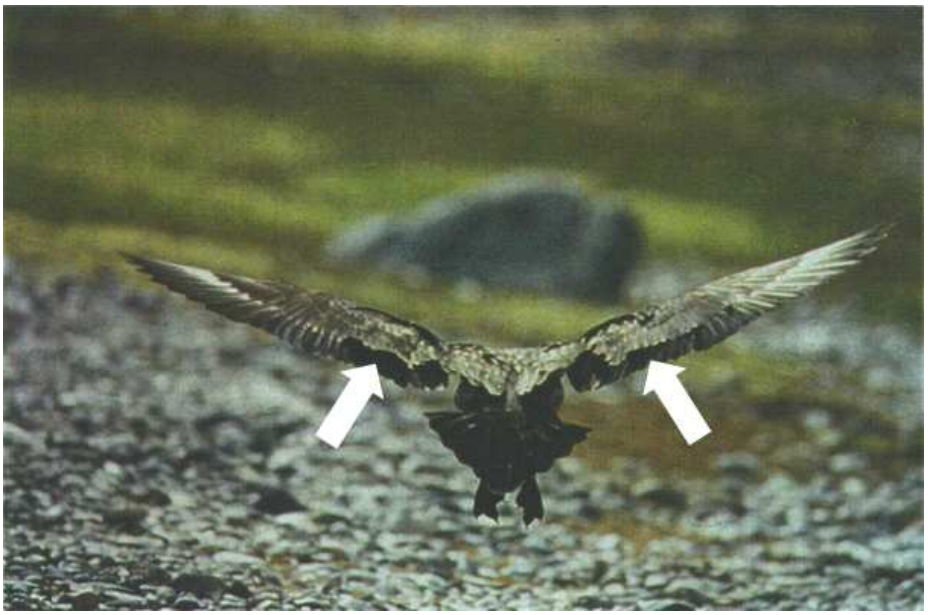

FIGURE 1.1. Skua wing in landing approach (photograph courtesy of Ingo Rechenberg).

Chapter 2

Control device and experimental setup

2.1. Model vehicle and control device

The model vehicle considered is the Ahmed body that is a representative fast-back type vehicle and is one of the most widely used models in studying the vehicle aerodynamics (figure 2.1). The Ahmed body is composed of a rounded fore-body to avoid flow separation there, a simple rectangular pillar-shaped middle-body and a slanted surface at the base. With this model, Ahmed *et al.* (1984) studied the effect of the rear slant angle (α) on the aerodynamic drag and the flow topology in the near wake. Figure 2.2 shows the variation of the drag coefficient with the slant angle (α), together with the schematic diagrams of the flow topology at different slant angles. For $0° \leqslant \alpha \leqslant 12.5°$, the flow remains attached to the slanted surface and separates at its rear edge. In this range, the drag decreases as the slant angle increases, and reaches the lowest at $\alpha = 12.5°$. For $12.5° < \alpha \leqslant 30°$, the flow separates at the front edge of the slanted surface but quickly reattaches, forming a separation bubble there that grows with increasing slant angle until $\alpha = 30°$. In this range, a pair of counter-rotating longitudinal vortices are developed from the lateral edges of the slanted surface, and their strength also increases with increasing slant angle, which is the main factor of the significant drag increase (called the induced drag) in this range (Hucho & Sovran 1993; Minguez *et al.* 2008; Choi *et al.* 2014). For $\alpha = 30°$, interestingly, there exist both high

and low drag regimes. In the high-drag regime, the strength of the longitudinal vortices reaches the highest, and the flow separated at the front edge of the slanted surface reattaches right before the rear edge. In the low-drag regime, however, the separation bubble on the slanted surface and the longitudinal vortices vanish, and the flow separates at the front edge of the slanted surface. Thus, the flow topology becomes similar to that at low slant angles (considering that the rear edge at low slant angle is not very different from the front edge at high slant angle) and closer to the flow over a square-back model, so the resultant drag is comparable to that at zero slant angle. These flow features have been discussed by Ahmed *et al.* (1984) and Choi *et al.* (2014). Note that the effect of the slant angle weakly depends on the Reynolds number (Bayraktar *et al.* 2001), so the slant angles and corresponding drag coefficients described above may change depending on the Reynolds number considered.

In the present study, we consider a half-scaled Ahmed body (figure 2.1) that provides a blockage ratio of about 6% in our experiment facility (see below). The length of the slanted surface (S) is $0.77H$ and the ground clearance (G) is $0.17H$, where H is the model height. We devise a rigid rectangular flat plate, as an AMD, similar to the one used in Bechert *et al.* (1997). This device can be made of any material as long as it is light and rigid. In the present study, we use transparent acrylic whose thickness (t) is 0.80 mm, mass per unit area (ρ_{AMD}) is 0.93 kg/m^2 and Young's modulus (E) is 2.47 GPa, and hard strawboard whose thickness is 1.24 mm, $\rho_{\mathrm{AMD}} = 0.70$ kg/m^2 and $E = 1.04$ GPa, respectively. We fix the width of AMD to be the same as the model width ($= Z$) and vary its longitudinal length ($0.63S \leqslant l \leqslant 0.99S$). The leading edge of this device is attached to the front edge of the slanted surface using a thin

cellophane tape because the uncontrolled flow starts to separate there, while its trailing edge is left to move freely (see figure 2.3). Beneath the trailing edge of this device, a few tiny protrusions with the height of less than 0.3 mm are installed to prevent it from completely clinging to the slanted surface, otherwise it might not readily pop up. As we show in the below, the AMD introduced in this section remains attached on the slanted surface at low free-stream velocities, but pops up automatically (passively) at high free-stream velocities and self-adjusts to a position where the aerodynamic lift force balances with its own weight. Therefore, we call this device an automatic moving deflector (AMD).

2.2. Experimental setup and measurement systems

The experiments are conducted in a closed-type wind tunnel (Göttingen type), whose test section is 0.9 m wide, 0.9 m high and 4 m long. The maximum wind speed in the test section is 60 m/s, and the uniformities of the mean streamwise velocity and turbulence intensity are both within 0.3% at the free-stream velocity (U_∞) of 20 m/s. To minimize the incoming boundary layer thickness, a raised floor, which is 2.8 m long, 0.9 m wide and 15 mm thick, is installed in the test section (figure 2.4). The leading edge of the raised floor is finished with a sandpaper to prevent flow separation. The mean streamwise velocity profile above the raised floor at $x'/H = 5.6$ (without the model) is measured using a hot-wire anemometry (HWA), where ($x' = 0$, $y' = 0$) corresponds to the location of the leading edge of the raised floor. At this location, the boundary layer thickness δ_{99} is about $0.090H$ ($= 0.52G$) and the displacement thickness δ^* is about $0.014H$ ($= 0.081G$). This value is so low (Hucho *et al.* 1975) that its effect on the aerodynamics around the model is negligible. The

blockage ratio due to the raised floor and model is 5.9%, which is smaller than the maximum value (7.5%) allowed to avoid the disturbances from the wind-tunnel wall (Barlow *et al.* 1999). The experiments are conducted at $Re_H = 1.0 \times 10^5 - 3.8 \times 10^5$.

The time-averaged drag on the model is measured using a one-axis load cell (AND LCB03K006M) whose measurement range is $0 - 6$ kgf, and maximum uncertainty is 0.02%. The output from the load cell is amplified and sampled for 90 s at a rate of 32 kHz to obtain a fully converged mean drag. The data from the measurement are transferred to a computer through an A/D converter (NI PCI-6251), after which they are post-processed. All the measurements are done with at least two independent runs. The drag coefficient (C_D) is defined as

$$C_D = \frac{D}{\frac{1}{2}\rho U_\infty^2 A_\mathrm{f}}, \tag{2.1}$$

where D is the time-averaged drag, ρ is the air density, and A_f is the frontal area (including the stilts) of the model. To measure the surface pressure at the slanted surface and vertical base of the model, 61 pressure taps are installed (36 on the slanted surface and 25 on the vertical base). The pressure taps are connected to a digital manometer (MKS 220D) having the measurement range of $0 - 10$ torr and the maximum uncertainty of 0.15%. At each measurement point, the pressure is measured for 90 s to obtain a fully converged mean value. The signals from the manometer are sampled at the rate of 10 kHz and transferred to a computer through an A/D converter (NI PCI-6251). The pressure coefficient (C_P) is defined as

$$C_P = \frac{P - P_\infty}{\frac{1}{2}\rho U_\infty^2}, \tag{2.2}$$

where P is the time-averaged surface-pressure, and P_∞ is the static pressure at the free-stream.

The velocity fields near the base of the model are measured using a particle image velocimetry (PIV). The schematic diagram of the experimental setup for the PIV measurement is presented in figure 2.5. Our PIV system consists of a fog generator (SAFEX), a double-pulsed Nd:YAG laser (Litron Lasers) operating at 135 mJ − 15 Hz, a CCD camera (Vieworks VH-4M) with a 2048 × 2048 pixel^2 resolution, and a timing hub (Integrated Design Tools). The fog generator produces liquid droplets of approximately 1 μm in diameter that are introduced into the wind tunnel. The laser illuminates the plane of interest with a 532 nm light sheet. The delay between two pulses is generated by the timing hub. Three (x, y) planes at $z/H = 0$, 0.27 and 0.54 and six (y, z) planes at $x/H = -0.10$, 0.25, 0.50, 0.75, 1.00 and 1.50 are considered for the measurement, where $x = 0$, $y = 0$ and $z = 0$ correspond to the locations of the vertical base, bottom surface, and spanwise centre, respectively. An iterative cross-correlation analysis is employed with an initial interrogation window size of 32 × 32 pixel^2 to obtain a final window size of 16 × 16 pixel^2 with an overlapping by 25%. The resultant spatial resolution is $0.0125H$ and $0.0144H$ in (x, y) and (y, z) planes, respectively, except for the (y, z) plane at $x/H = -0.10$ at which the resolution is $0.0071H$. To obtain a fully converged mean velocity field, 2000 instantaneous fields are taken and averaged at each plane.

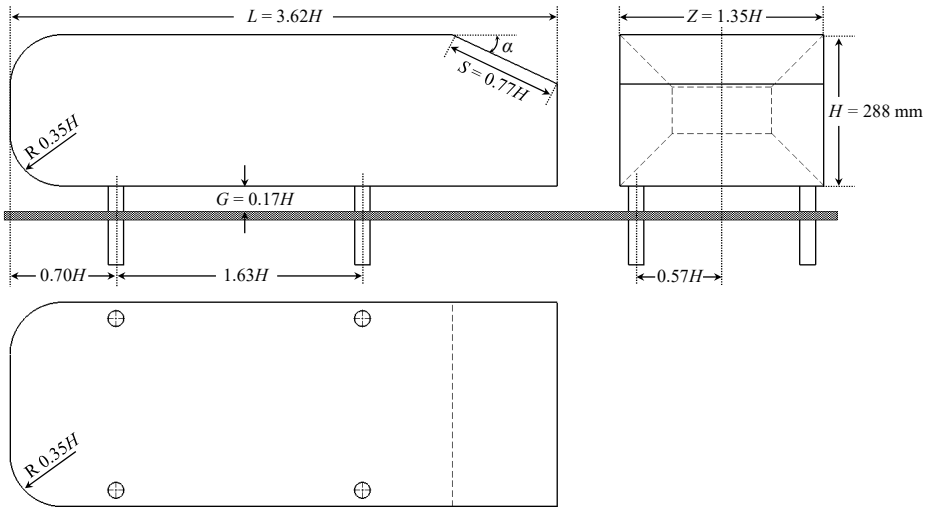

FIGURE 2.1. Ahmed body (redrawn from Ahmed *et al.* 1984).

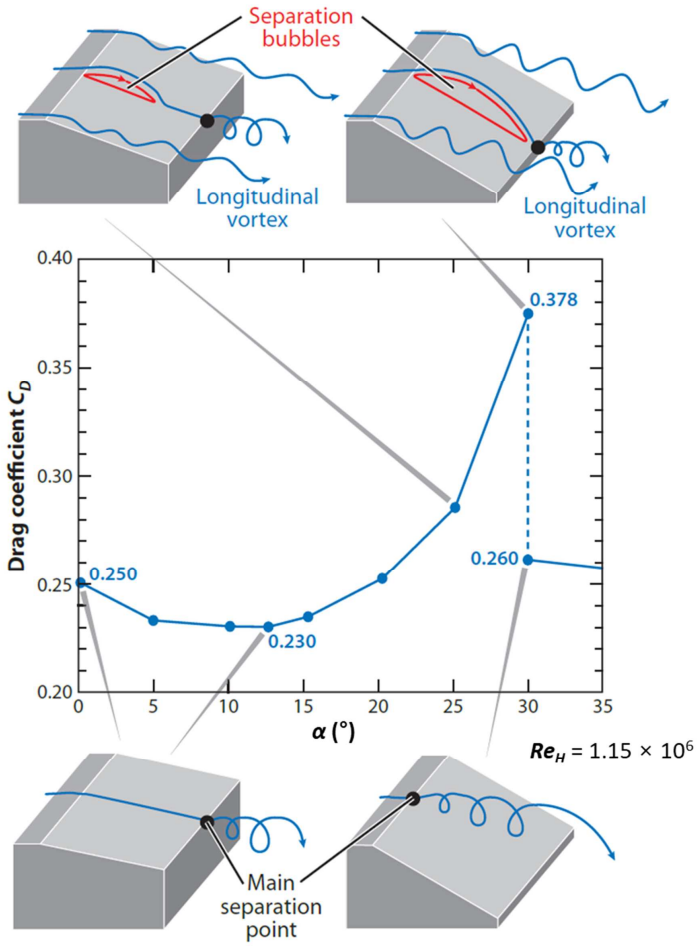

FIGURE 2.2. Variation of the drag coefficient of the Ahmed body with the slant angle at $Re_H = 1.15 \times 10^6$ (Ahmed *et al.* 1984, from Choi *et al.* 2014).

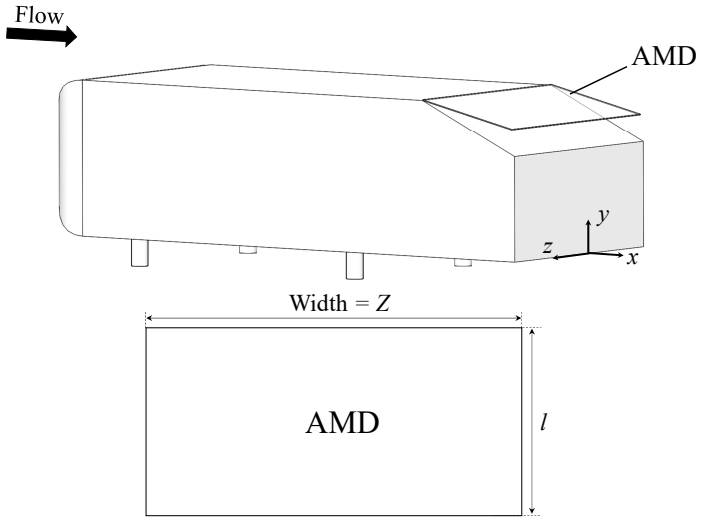

FIGURE 2.3. AMD attached on the Ahmed body and its geometric configuration.

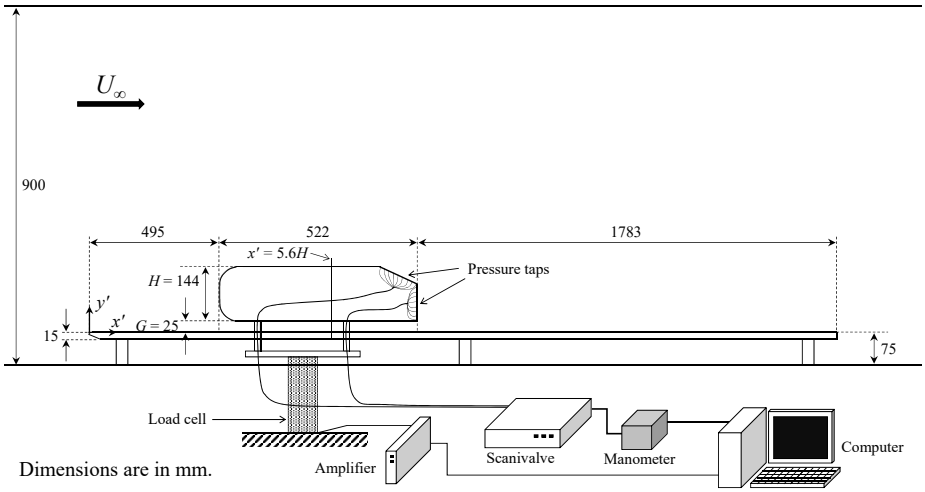

FIGURE 2.4. Schematic diagram of the experimental setup for the drag and surface-pressure measurements.

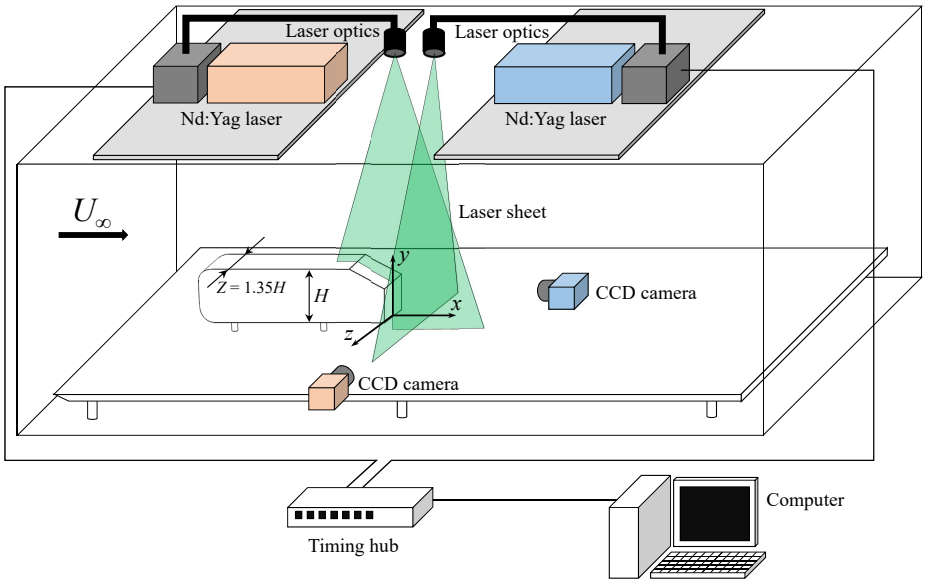

FIGURE 2.5. Schematic diagram of the experimental setup for the PIV measurement.

Chapter 3

Results and discussion

3.1. Drag variation

Figure 3.1 shows the variation of the drag coefficient with the slant angle at three different Reynolds numbers, together with those from previous experiments at similar Reynolds numbers. The drag coefficients measured in the present study are in agreements with those of previous studies. With increasing Reynolds number, the drag coefficient decreases. As the slant angle increases, the drag coefficient first decreases and reaches minimum at $\alpha = 10°$, and then increases and reaches maximum at $\alpha = 25°$. This behaviour agrees very well with the previous observations (Ahmed *et al.* 1984; Conan *et al.* 2011). At $\alpha = 30°$, unlike Ahmed *et al.* (1984), the present measurement shows only the low-drag regime. According to the previous studies, the low-drag regime appears in higher probability than the high-drag regime. For example, Ahmed *et al.* (1984) indicated that the high-drag regime was not maintained over a long period of time and low drag regime was more stable, because merging of the separation bubble above the slanted surface to main separation by insignificant disturbances in the incoming flow resulted in the switch over the low-drag regime. Conan *et al.* (2011) also reported that the low-drag regime occurs three-times more frequently than the high-drag regime. For the present control purpose, we choose the slant angle of $\alpha = 25°$ at which the drag coefficient is highest.

Figure 3.2 shows the variations of the drag reduction rate, $\Delta D = (D_{\mathrm{NO}} - D_{\mathrm{AMD}})/D_{\mathrm{NO}} \times 100$, with the length ($l$) of AMDs made of transparent acrylic and hard strawboard at three different Reynolds numbers, where D_{NO} and D_{AMD} are the drags without and with AMD, respectively. We separately measured the drags on the Ahmed body with 'inactive' AMD (i.e., AMD is attached on the model but is locked not to pop up) at $\alpha = 25°$ and three different Reynolds numbers, and found that the drags measured are different by less than 1.5% from those without AMD (D_{NO}), indicating that the inactive AMD itself little changes the flow near the slanted surface. As shown in figure 3.2, the drag is reduced significantly by AMD. This reduction comes from the modification of the flow separation points from the front edge of the slanted surface to the trailing edge of AMD (see below). For the case of AMD made of transparent acrylic (figure 3.2(a)), at $Re_H = 1.9 \times 10^5$ and 2.9×10^5, ΔD increases with increasing l, reaching maximum drag reduction of about 17.5%. On the other hand, at $Re_H = 3.8 \times 10^5$, ΔD decreases from $l/S = 0.72$. This comes from the vertical fluttering of the acrylic AMD at high free-stream velocity due to its relatively weak bending stiffness: massive vibration occurs at $l/S \geq 0.81$ and drops its drag-reduction performance. This fluttering does not occur for the AMD made of hard strawboard, since its bending stiffness or flexural rigidity (EI; I ($= t^3Z/12$) is the second moment of area) is 1.57 times that of the AMD made of acrylic (on the other hand, no significant spanwise fluttering is observed for both AMDs). Thus, the drag-reduction rate for the case of hard-strawboard AMD increases with increasing l and Re_H for all the Reynolds numbers considered (figure 3.2(b)), although there is a slight decrease in ΔD for $l/S = 0.99$ at $Re_H = 3.8 \times 10^5$. Note that the amounts of drag reduction with the hard-strawboard AMD (up

to 19%) are slightly larger than those of the transparent-acrylic AMD (17.5%). This improvement with the hard-strawboard AMD is attributed to its lighter mass by 25% that enables the AMD to lift higher; e.g., at $Re_H = 2.9 \times 10^5$, the lift angle of the hard-strawboard AMD from the slanted surface is about 17.5°, whereas that of the transparent-acrylic AMD is about 16.5°. This different lift angle of AMD locates the spanwise vortex in a different position in the wake, which changes the pressure distribution on the slanted surface. As mentioned previously, Fourrié *et al.* (2011) attached a non-movable flap to the front edge of the slanted surface at the slant angle of 25° and measured the drag force for various deflection angles (defined by the angle from the slanted surface). They obtained drag reduction of 9% when the deflection angle θ was 30°, but the drag was increased by 5.6% when $\theta = 18°$ (similar to our case). This is because their flap length is much shorter ($l = 0.09S$) than that of the present study. Beaudoin & Aider (2008) also reported drag reductions for different control parameters, but reported a drag increase of 7.7% when a non-movable short flap ($l = 0.07S$) was applied for the condition similar to the present one. In the following section, we discuss the modifications of the flow characteristics by the transparent-acrylic AMD which allows us to measure the flow in between the slanted surface and AMD.

3.2. Operating mechanism of AMD

In this section, we investigate when and why AMD pops up by analysing the dynamics of AMD at the initial stage of its operation for the case of $l/S = 0.90$ where the drag reduction was high. The present AMD made of transparent acrylic starts to pop up at $Re_H \approx 1.2 \times 10^5$. To understand how this AMD starts to pop up, the pressure distributions on the upper

and lower surfaces of AMD should be known. However, direct measurements of pressure on its surfaces are impossible because it is very thin. Therefore, an indirect measurement of the surface pressures is devised here. At $Re_H = 1.0 \times 10^5$ (just before pop-up), AMD stays attached on the slanted surface (i.e., AMD is inactive). Then, the pressure on the slanted surface in the absence of AMD may be considered as the pressure on the upper surface of AMD in its presence. On the other hand, in the presence of AMD, the pressure on the slanted surface (note that there exists a very thin gap between the slanted surface and AMD lower surface) may be taken as the pressure on the lower surface of AMD considering very thin gap between two surfaces. This argument is supported by the negligible difference in the drags with inactive AMD and without AMD, as described in section 3.1.

Figures 3.3(a) and (b) show the contours of the mean pressure coefficients on the lower and upper surfaces of inactive AMD that are converted from the pressures on the slanted surface at $Re_H = 1.0 \times 10^5$. The pressure difference between the upper and lower surfaces is given in figure 3.3(c), which provides the lift force (or counter-clockwise rotation) on AMD. As shown, most of the lift force on AMD is generated near its leading-edge and centre regions. This is because, in the presence of AMD, the slanted surface is not influenced by low pressure from flow separation occurring at the leading edge of AMD.

Assuming that the pressure distributions on the AMD surfaces at the time of pop-up are not so different from those in figure 3.3, one can predict the critical free-stream velocity at which AMD of $l/S = 0.90$ pops up,

considering the torque balance, $T_P \approx T_{\mathrm{AMD}}$ (figure 3.3):

$$\frac{\rho U_\infty^2}{\rho_{\mathrm{AMD}} g} = \frac{l^2 \cos\alpha}{\displaystyle\int_0^l \xi (C_{P\mathrm{l}} - C_{P\mathrm{u}}) \mathrm{d}\xi} \approx 20.5, \tag{3.1}$$

where ρ_{AMD} is the mass per unit area of AMD. For the present AMDs ($\rho_{\mathrm{AMD}} = 0.93$ and 0.70 kg/m^2 for transparent acrylic and hard strawboard, respectively), the critical free-stream velocities for the pop-up are about 12.4 and 10.8 m/s, respectively, corresponding to $Re_H = 1.19 \times 10^5$ and 1.04×10^5. Once the AMDs made of transparent acrylic and hard strawboard pop up, they return to their initial position when the free-stream velocities are reduced to 11.1 and 9.6 m/s, respectively, which are slightly lower than the critical velocities for the pop-up. This is probably due to the presence of reverse flow in the gap between the slanted surface and AMD, providing additional lift force to AMD.

Figure 3.4 shows the time sequence of the flow fields during the pop-up ($Re_H = 1.2 \times 10^5$), where each time interval is about 0.12 s. Before the pop-up, the flow massively separates from the front edge of the slanted surface (figure 3.4(a)) and a strong longitudinal vortex exists on its lateral side (figure 3.4(d)), which produces low pressure regions at the front edge and lateral side of the slanted surface (see, for example, figure 3.3(b)). After the pop-up, the flow attaches to the AMD surface (figure 3.4(c)) and the separation point is delayed to the trailing edge of AMD. The longitudinal vortex existed at the lateral side is shifted upward and slightly outward with its reduced strength during the pop-up (figures 3.4(e) and (f); see also later in this paper). After the pop-up, a weak reverse flow exists in the gap between the slanted surface and AMD, making it keep afloat (see below).

3.3. Drag-reduction mechanism

We investigate the mechanism responsible for drag reduction by AMD for the case of $l/S = 0.90$ at $Re_H = 2.9 \times 10^5$, where $\Delta D = 17.5\%$. Figure 3.5 shows the changes in the mean streamwise velocity and the mean streamlines due to AMD at three different (x, y) planes. Without AMD, the flow separates at the front edge of the slanted surface but reattaches near its rear edge, forming a separation bubble there (figures 3.5(a) and (c)). Then, main separation occurs at the rear edge of the slanted surface. Since a separation bubble induces a low-pressure region around itself, it significantly drops the pressure at the upper part of the slanted surface (figure 3.6(a)), resulting in a significant drag increase. Note that the pressure at the lower part is recovered owing to the flow reattachment. Meanwhile, the flow at $z/H = 0.54$ does not separate (figure 3.5(e)) because the strong longitudinal vortex emanating from the lateral side of the slanted surface induces downwash momentum there, but the pressure there is still reduced (called induced drag; figure 3.6(a)).

With AMD, the flow remains attached to its upper surface, and a weak reverse flow exists in the gap between the slanted surface and AMD (figures 3.5(b), (d) and (f)). Therefore, the pressure on the slanted surface is exposed to the flow in the wake rather than the flow above the AMD. As a result, the pressure level on the slanted surface is not very different from that on the vertical base surface, and thus the pressure is considerably recovered from that without AMD (figure 3.6(b)). On the other hand, the pressure level on the vertical base surface with AMD is comparable to that without AMD. As shown in figure 3.5, the main separation bubble with AMD is stronger and larger but locates farther than that without AMD, resulting in similar pressure levels on the vertical base surface for

both cases. Therefore, the drag reduction caused by AMD is mainly from the pressure recovery on the slanted surface.

Figure 3.7 shows the streamwise evolutions of the mean cross flow without and with AMD. Without AMD, a pair of longitudinal vortices are developed from the lateral sides of the slanted surface and move downstream. The intensity of the swirling motion by these vortices decreases in downstream but they survive even after $x/H = 1.50$. However, with AMD, the longitudinal vortices are considerably weakened and almost disappear even in near-wake region, leading to a significant reduction in the induced drag by AMD. Owing to AMD, the magnitudes of the Reynolds normal and shear stresses are also significantly reduced (figures 3.8 and 3.9). Without AMD, they are large near the slanted surface and the vertical base, respectively, due to the separating shear layer and the longitudinal vortices. With AMD, large Reynolds stresses disappear above the slanted surface and are delayed farther downstream in the wake with reduced strengths. These reduced Reynolds stresses contribute to the reduction of drag.

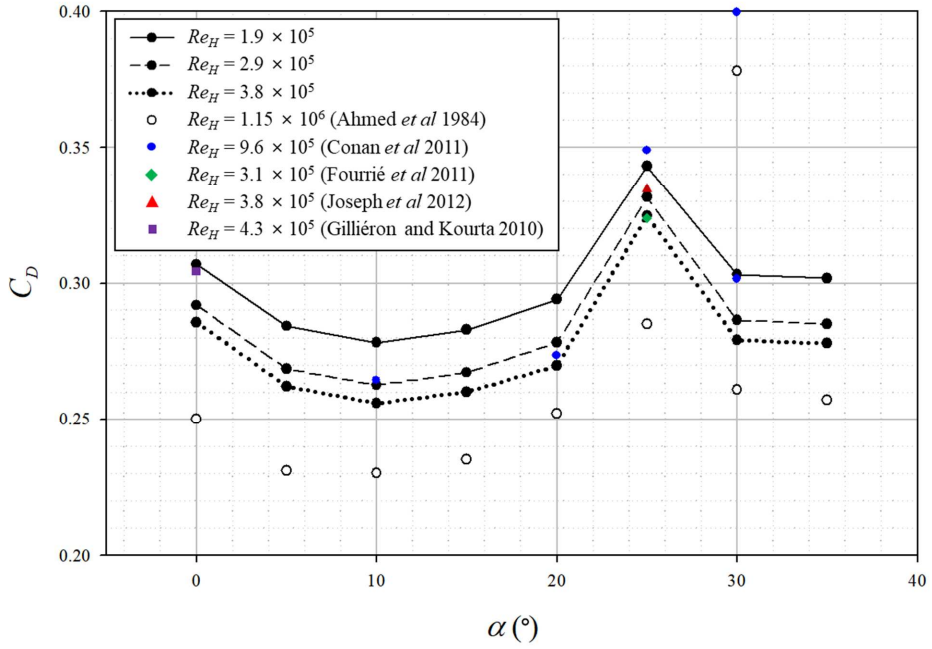

FIGURE 3.1. Variation of the drag coefficient with the slant angle.

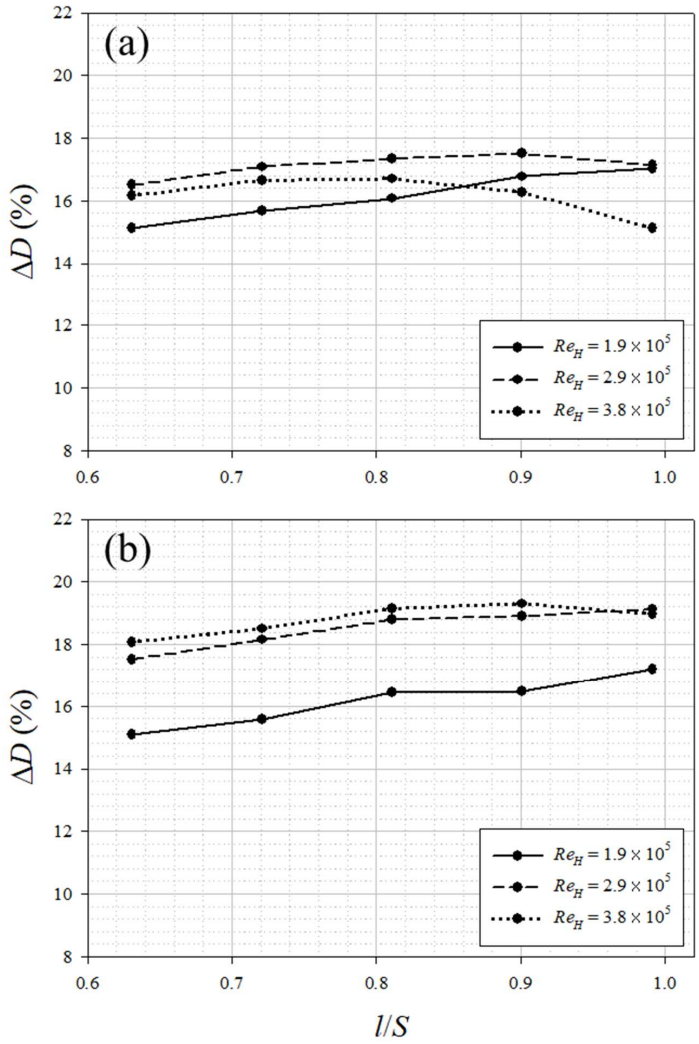

FIGURE 3.2. Variations of the drag reduction rate with the length of AMDs made of (a) transparent acrylic and (b) hard strawboard.

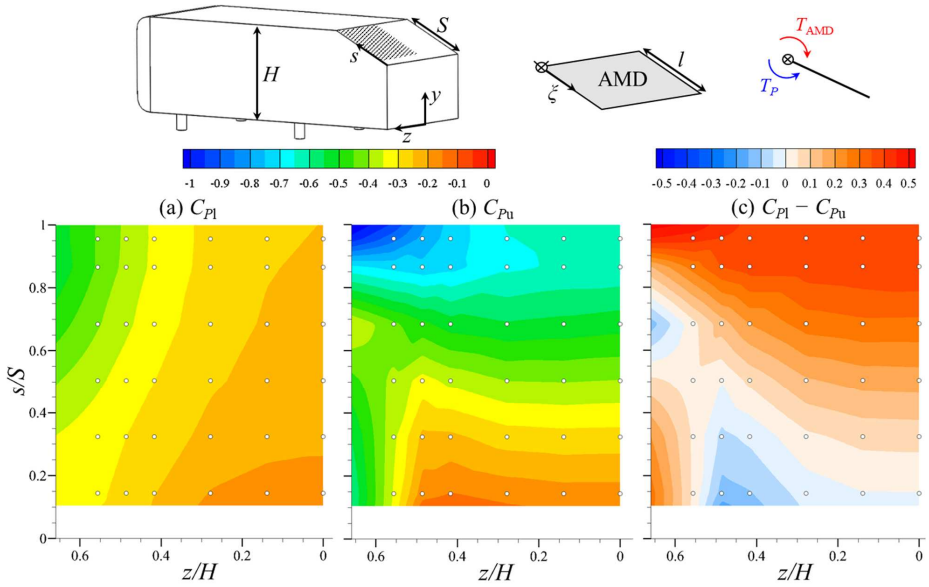

FIGURE 3.3. Contours of the mean pressure coefficient on the AMD surfaces ($Re_H = 1.0 \times 10^5$): (a) lower surface; (b) upper surface; (c) their difference. Note that the pressures are measured on the slanted surface of the Ahmed body and converted to those on the AMD surfaces. White circles in this figure denote the locations of the pressure measurement.

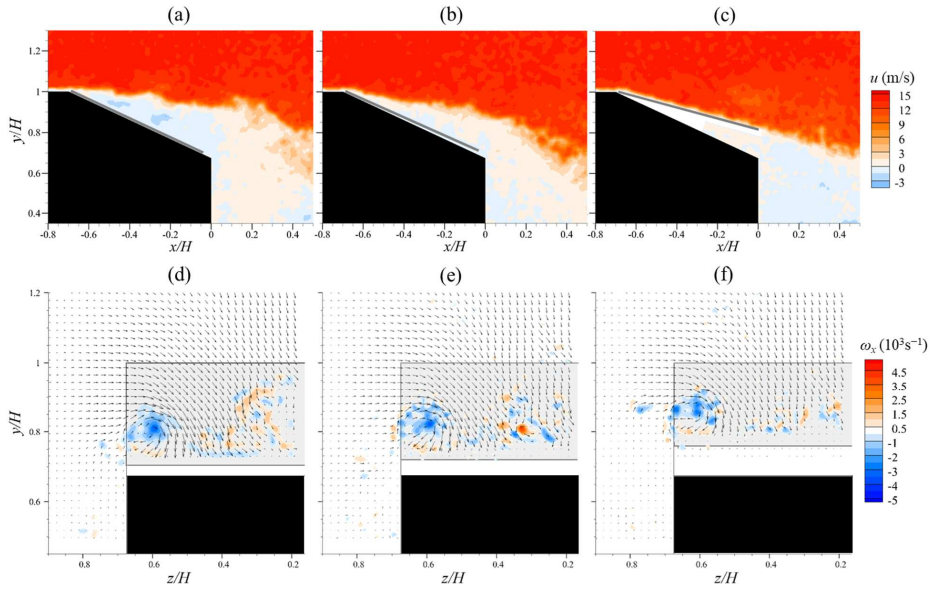

FIGURE 3.4. Contours of the instantaneous streamwise velocity at the centre plane ($z/H = 0$) (upper) and the contours of the instantaneous streamwise vorticity together with the instantaneous velocity vectors on a cross-flow plane ($x/H = -0.10$) (lower) ($Re_H = 1.2 \times 10^5$). Here, (a – c) and (d – f) show the time sequence: before, during, and after the pop-up (left to right). The locations of AMD are shown in black lines.

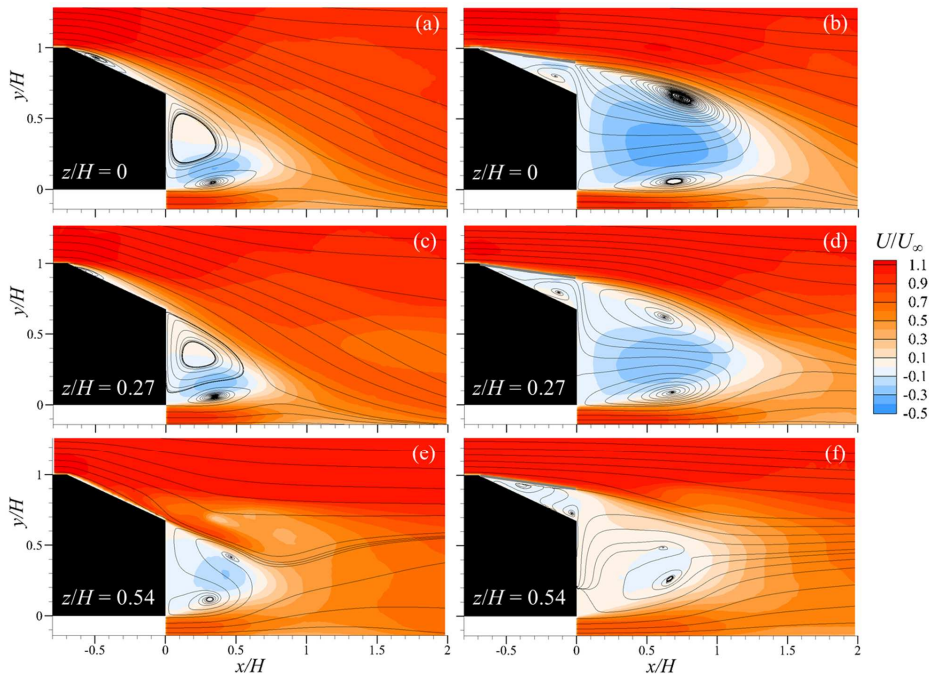

FIGURE 3.5. Contours of the mean streamwise velocity and the mean streamlines at (x, y) planes without (a, c, e) and with AMD (b, d, f). $Re_H = 2.9 \times 10^5$.

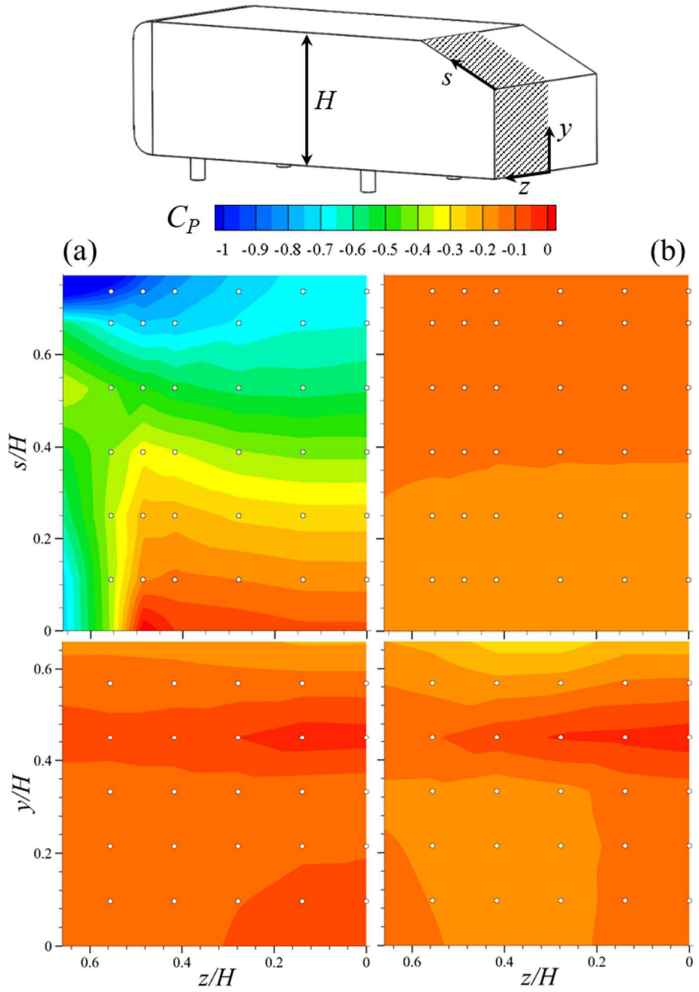

FIGURE 3.6. Contours of the mean pressure coefficient on the left halves of the slanted (upper) and vertical base (lower) surfaces ($Re_H = 2.9 \times 10^5$): (a) without AMD; (b) with AMD. White circles in this figure denote the locations of the pressure measurement.

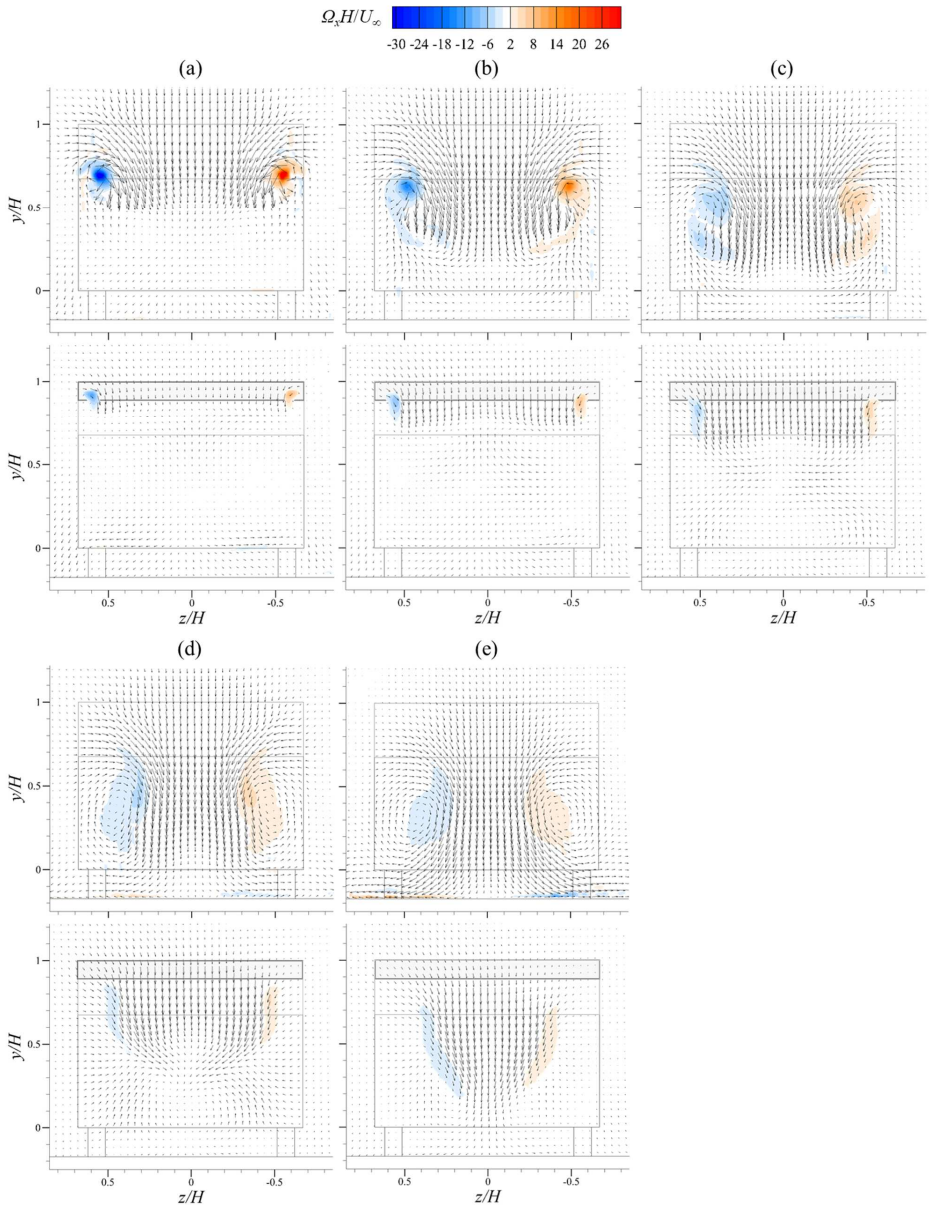

FIGURE 3.7. Secondary flows in the wake: contours of the mean streamwise vorticity and the mean velocity vectors on the cross-flow planes without (upper) and with AMD (lower). (a) $x/H = 0.25$; (b) 0.50; (c) 0.75; (d) 1.0; (e) 1.5.

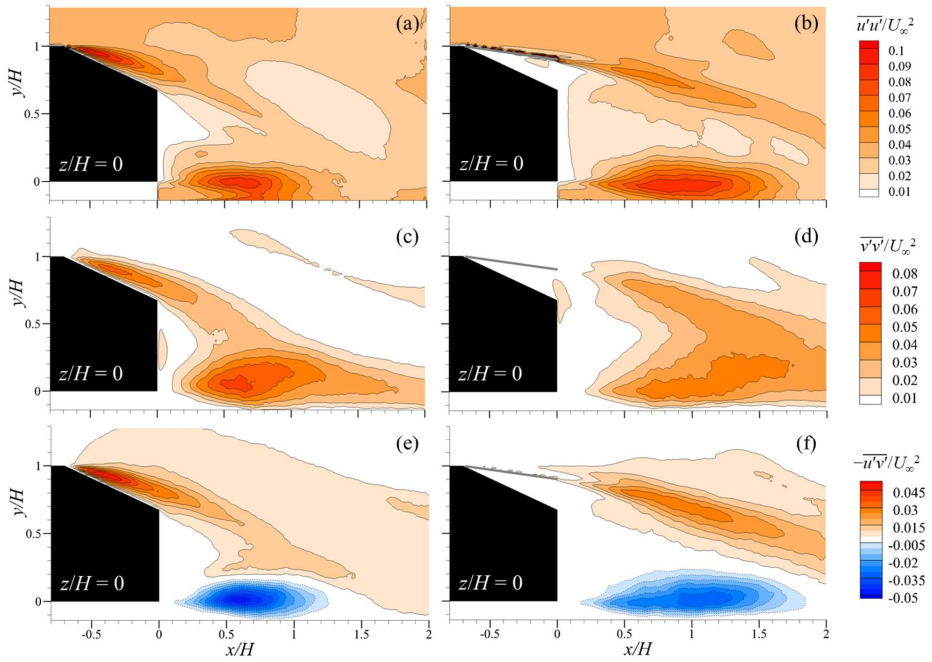

FIGURE 3.8. Contours of the Reynolds stresses on the (x, y) plane at $z/H = 0$ without (a, c, e) and with AMD (b, d, f). (a, b) $\overline{u'u'}/U_\infty^2$; (c, d) $\overline{v'v'}/U_\infty^2$; (e, f) $-\overline{u'v'}/U_\infty^2$.

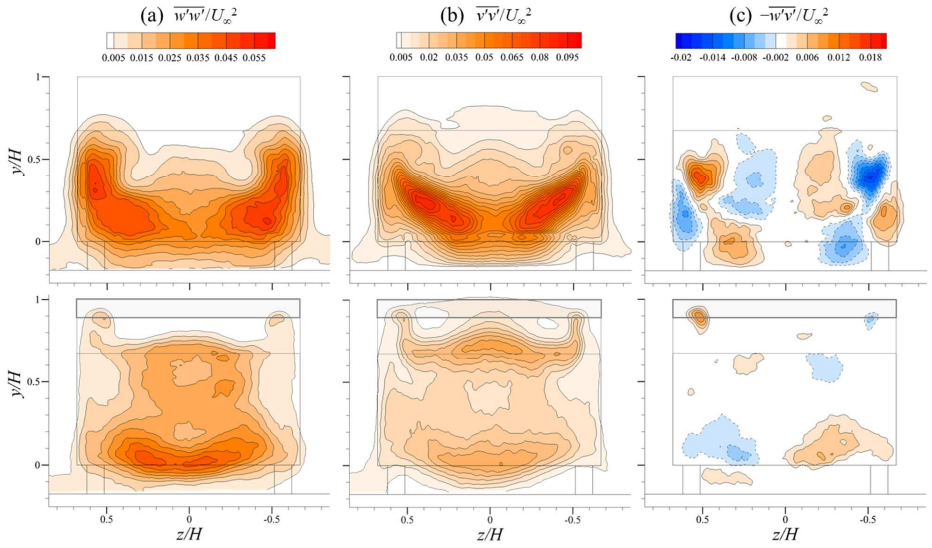

FIGURE 3.9. Contours of the Reynolds stresses on the cross-flow plane at $x/H = 0.75$ without (upper) and with AMD (lower). (a) $\overline{w'w'}/U_\infty^2$; (b) $\overline{v'v'}/U_\infty^2$; (c) $-\overline{w'v'}/U_\infty^2$.

Chapter 4

Conclusions

In the present study, we experimentally investigated the drag reduction of a three-dimensional model vehicle (Ahmed body) by introducing a biomimetic flow control device inspired by the secondary feathers of a bird's wing (called AMD in this study). The aerodynamic performance of the AMD was examined through the measurements of the drag force, surface pressure and velocity field near and behind the base surface of the Ahmed body. The AMD significantly reduced the drag on the Ahmed body, and its performance was enhanced with AMD made of lighter and stiffer material, such as hard strawboard. With this AMD, by varying its longitudinal length, drag reduction of maximum 19% was achieved. It was shown from the dynamics of AMD at the initial stage of its operation that it starts to pop up when the pressure in the thin gap between the slanted surface and AMD becomes much larger than that on the upper surface of AMD. Without AMD, at the slant angle of 25°, a separation bubble existed above the slanted surface and strong counter-rotating longitudinal vortices were developed along the lateral sides of the slanted surface. These flow structures induced low pressure regions on the slanted surface, particularly at its front edge and lateral sides, resulting in a high drag. On the other hand, the AMD prevented the formation of the separation bubble above the slanted surface by delaying the separation point to the trailing edge of AMD, and suppressed the strength of the longitudinal

vortices. These flow modifications by AMD resulted in substantial reductions of the Reynolds stresses and pressure recovery at the slanted surface, leading to a significant drag reduction.

The AMD introduced in this study is an effective flow control device because it is a passive device (no external power required to operate) and little changes the body shape when it does not operate. The AMD operates only when the flow speed is sufficiently high such that flow separation occurs above the slanted surface. The concept of the present device may be applicable to road vehicles. For example, the present AMD may be applicable to some passenger cars having fastbacks like sedans that have slant angles from 20° to 27°. Hatchback and SUV models having similar slant angles may also have some benefits from the application of AMD. Its applications may be further extensible to some parts of fluid machinery containing massive flow separation, such as the diffuser and combustor.

Part II.

Drag reduction on a three-dimensional model vehicle by an active flow control

Chapter 1

Introduction

Reducing the aerodynamic drag on a road vehicle has always been an important issue both in academia and industries, because it directly leads to a reduction of fossil fuel consumption and thereby to a reduction of environmental contaminant emission. Bellman *et al.* (2010) reported that 53% of total fuel consumption of ground vehicles in U.S. goes into overcoming the aerodynamic drag and thus 15% reduction in the drag at highway speed (≈ 90 km/h) would lead to fuel saving of $5-7\%$. The aerodynamic drag of heavy vehicles is especially even more crucial in the fuel economy due to their relatively higher drag coefficient than that of generic passenger cars (*Robert Bosch GmbH*, 2002). For example, McCallen *et al.* (1999) reported that a typical modern tractor-trailer possessing the drag coefficient of 0.6 takes 65% of the total fuel consumption from overcoming the aerodynamic drag. They suggested that reducing the drag coefficient from 0.6 to 0.3 for a typical tractor-trailer would result in a 43% fuel saving. Therefore, many studies have considered both passive and active means (see, for a review, Choi *et al.* (2014)) for the drag reduction on a model vehicle, most of which have adopted the Ahmed body (Ahmed *et al.* 1984) as a representative simplified model for heavy vehicles.

Passive flow controls have mainly been conducted with vortex generators, flaps or a splitter plate. For example, Pujals *et al.* (2010) attached an array of cylindrical vortex generators on the rear edge of the roof of

the Ahmed body at the slant angle of 25° and acquired about 10% drag reduction. Krajnović (2014) also conducted a follow-up study of Pujals *et al.* (2010) using numerical simulation and obtained a similar result. Beaudoin & Aider (2008) applied flaps to the edges of the rear part of a modified Ahmed body at the slant angle of 30° and obtained up to 25% drag reduction. Fourrié *et al.* (2011) also used a flap attached to the front edge of the slanted surface of the Ahmed body with various deflection angles and obtained drag reductions up to 9%. Gilliéron & Kourta (2010) installed a splitter plate behind the square-back Ahmed body and they obtained up to 12% drag reduction. Apart from these techniques applying fixed appendages, Kim *et al.* (2016) introduced a bio-inspired device called an automatic moving deflector which automatically (i.e. without external power input) popped up when the flow separated from the front edge of the slanted surface. They obtained up to 19% drag reduction with this movable deflector. These passive control devices are powerful and efficient because they are readily applicable and need no external power. However, these passive devices inevitably require appendages on the model surface or even a shape modification of the vehicle model and may not perform well at various vehicle speeds.

On the other hand, many active flow controls have been conducted mainly by fluidic blowing/suction devices with steady and unsteady operations. For example, Rouméas *et al.* (2009) performed a steady suction on the front edge of the slanted surface to suppress the flow separation there and obtained about 17% drag reduction. Recently, Zhang *et al.* (2018) applied a steady blowing from the edges of the rear part of the Ahmed body, analogous to the passive device of Beaudoin & Aider (2008), and obtained up to 29% drag reduction by controlling each actuator indi-

vidually. As for unsteady controls, Joseph *et al.* (2012) and Gilliéron & Kourta (2013) also obtained about 8% and 20% drag reductions, respectively, by periodic forcing with pulsed jets applied near the front edge of the slanted surface of the Ahmed body. Kourta & Leclerc (2013) and Tounsi *et al.* (2016) obtained up to 9% and 10% drag reductions, respectively, by periodic blowing and suction with synthetic jets installed at similar positions. Furthermore, Barros *et al.* (2016) obtained 11% drag reduction with pulsed jets attached at the four edges of the vertical base of the square-back Ahmed body and enhanced their performance together with the Coanda effect, resulting in up to 18% drag reduction. Although above-mentioned blowing/suction devices are well suitable for the vehicle flow control, they may not be easily applicable in practice because they often require an external fluid source/sink and even a rather complicated apparatus for operating them.

As an alternative active flow control technique, the plasma actuator, or more precisely dielectric barrier discharge (DBD) actuator, has received a great attention since the first pioneering work by Roth *et al.* (1998) owing to its several remarkable features that conventional active control devices lack: fully electronic with a simple structure, no additional holes or cavities required, very low mass and thickness ($O(100\ \mu\mathrm{m})$ in general), fast time response ($O(1\ \mathrm{ns})$), capable of a broad range of driving frequency (up to $O(10\ \mathrm{kHz})$), etc. figure 1.1 shows a basic structure of a typical DBD plasma actuator. It consists of a pair of asymmetrically arranged electrodes, where the upper one is exposed and the lower one is encapsulated by a dielectric layer. The dielectric layer is usually made of polymers, for example, Kapton, Teflon or acrylic, but it can also be made of glasses or ceramics. During operation, the exposed electrode is

provided with a high voltage waveform, either alternating or pulsed, while the encapsulated electrode is electrically grounded in general. When the exposed electrode is applied with a high enough voltage waveform (a few kV in general), air molecules over the encapsulated electrode are weakly ionized by collisions mainly with the emitted electrons from the edge of the exposed electrode and the upper surface of the dielectric layer. The ionized air emits a weak visible light so that it appears purple when seen by naked eyes. Then, the ionized air exerts momentum to the ambient air, as a form of body force, by the strong electric field formed between the electrodes. See Corke *et al.* (2010), Benard & Moreau (2014) and Kotsonis (2015) for further information on the fundamental characteristics of the plasma actuator.

A few studies have been conducted on the drag reduction on a model vehicle typically with AC-DBD actuators. Boucinha *et al.* (2011) was the first to introduce plasma actuators to a model vehicle (Ahmed body). They obtained up to 8% drag reduction by applying them on the slanted surface in several configurations with and without an input signal modulation. Julian *et al.* (2016) attached plasma actuators on the front edges of the roof and slanted surface of the Ahmed body with 30° slant angle, and obtained up to 22% drag reduction but at very low Reynolds number of $Re_H = 8{,}160$. Shadmani *et al.* (2018) also applied a plasma actuator on the front edge of the slanted surface of the Ahmed body with and without an input signal modulation, and obtained up to 7% drag reduction. Khalighi *et al.* (2016) attached plasma actuators on the rear edges of a modified square-back Ahmed body, and they achieved up to 21% drag reduction. Other than these conventional plasma actuator (linear type), some researchers reported notable results with the streamwise actuators

(so-called plasma streamwise vortex generator; PSVG). Roy *et al.* (2016) obtained up to 15% drag reduction on a realistic tractor-trailer model with PSVGs installed near the rear edges. Vernet *et al.* (2018) also applied the PSVG on a lateral side of the front head of a realistic tractor-trailer model and obtained the increase in the drag reduction up to 20% with increasing yaw angle.

Although these recent studies suggested the DBD plasma actuator as an effective control device for a ground vehicle drag reduction, detailed flow modifications due to control have not been fully investigated. Thus, a more extensive study on the flow field is required for understanding the drag reduction mechanism. Besides, further development and optimization of the plasma actuator are still needed for higher drag reduction and efficiency. One way to enhance the performance and efficiency of the plasma actuator may be to replace the exposed electrode with a thin wire whose diameter is as small as $O(10\ \mu\text{m})$. Hoskinson & Hershkowitz (2010) observed the plasma structure from the wire-to-plate actuator with varying the diameter of the wire electrode. They found that filamentary microdischarges, which dissipate a substantial amount of electric power, starts to disappear when the wire diameter is less than 130 μm, and they get almost extinguished as the diameter further decreases. Then, the power dissipation by the actuator is reduced by 40% with a 25 μm wire. Furthermore, Debien *et al.* (2012*a*) compared the phase-averaged induced velocity by a wire-to-plate actuator (wire diameter of 13 μm) with that by a plate-to-plate actuator and showed that the former is much larger (about twice) than the latter. Nevertheless, there has been no study on the application of this wire-to-plate DBD plasma actuator to an aerodynamic model for flow control.

Therefore, in the present study, we apply this wire-to-plate DBD plasma actuator to the Ahmed body by varying the spanwise length of the actuator and applied voltage, and compare its performances with those of a conventional plate-to-plate DBD plasma actuator. We measure the changes in the drag on the Ahmed body and the power consumption. The mechanism responsible for the drag reduction is also investigated by measuring the velocity fields above the slanted surface and behind the vertical base surface using a particle image velocimetry (PIV) and the surface pressure on the slanted and vertical base surfaces.

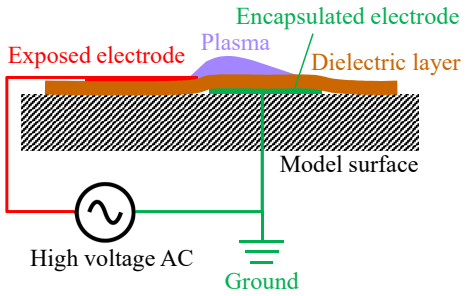

FIGURE 1.1. Schematic diagram of a typical DBD plasma actuator.

Chapter 2

Experimental details

2.1. Model vehicle

The model vehicle considered is the Ahmed body which is one of the most widely used models in studying the vehicle aerodynamics (figure 2.1). The Ahmed body is composed of a rounded fore-body (to avoid flow separation there), a simple rectangular pillar-shaped middle-body, and a slanted surface at the base. With this model, Ahmed *et al.* (1984) studied the effect of the rear slant angle (α) on the aerodynamic drag and the flow topology in the near wake. See Choi *et al.* (2014) for more details on the variation of the flow characteristics with the slant angle.

In the present study, we employ a half-scaled Ahmed body (figure 2.1) that provides a blockage ratio of 5.9% in our experiment facility (see section 2.3). For the present control purpose, we set the slant angle of $\alpha = 25°$, at which the drag is highest under our experimental setup (see Kim *et al.* (2016) for more details). The length of the slanted surface (S) is $0.771H$ and the ground clearance (G) is $0.174H$, where H is the model height.

2.2. DBD plasma actuator and power supply system

The plasma actuator used in the present study consists of exposed and encapsulated electrodes made of 11 μm tungsten wire and copper tape of 78 μm thickness, respectively, and a dielectric layer made of 2

layers of Kapton film whose thickness is 110 μm each. The width of the encapsulated electrode is 10 mm that is the shortest length providing enough induced momentum (Qi *et al.* 2016). The actuator is installed at the edge between the roof and slanted surfaces of the Ahmed body such that the intersection line of the two electrodes locates at this edge (the gap between the electrodes is zero) (figure 2.2). The spanwise length of the actuator varies from $l = 0.4Z$ to Z, and its center locates at the center of the vehicle model.

A high-voltage sinusoidal signal driving the plasma actuator is generated by a high-voltage AC power supply (Amazing1 PVM500-4000) whose maximum output with a non-resonant load is 300 W (40 $\mathrm{kV_{p-p}}$, 18 $\mathrm{mA_{peak}}$), operating at $20-70$ kHz. To obtain highest voltage, the input frequency is always set to be the lowest (20 kHz). With an AWG18 1.4 m long high-voltage cable, the resultant maximum applied voltages (V_a) in the present setup are from 9 to 11 $\mathrm{kV_{p-p}}$ depending on the actuator length.

2.3. Experimental setup and measurement system

The present experiments are conducted in a closed-type wind tunnel (Göttingen type), whose test section is 0.9 m wide, 0.9 m high, and 4 m long. The maximum wind speed in the test section is 60 m/s, and the uniformities of the mean streamwise velocity and turbulence intensity are both within 0.3% at the free-stream velocity (U_∞) of 20 m/s. To minimize the incoming boundary layer thickness, a raised floor, which is 2.8 m long, 0.9 m wide and 15 mm thick, is installed in the test section (figure 2.3). The leading edge of the raised floor is finished with a sandpaper to prevent flow separation. The mean streamwise velocity profile above the raised

floor at $x'/H = 5.6$ (without the model) is measured using a hot-wire anemometry (HWA), where ($x' = 0$, $y' = 0$) corresponds to the location of the leading edge of the raised floor. At this location, the boundary layer thickness δ_{99} is about $0.0903H$ ($= 0.520G$) and the displacement thickness δ^* is about $0.0140H$ ($= 0.0808G$). Therefore, the incoming boundary layer little affects the flow over the Ahmed body. The blockage ratio due to the raised floor and model is 5.9%, which is smaller than the maximum value (7.5%) allowed to avoid the disturbances from the wind-tunnel wall (Barlow *et al.* 1999). The experiments are conducted at $Re_H = U_\infty H/\nu = 0.96 \times 10^5, 1.44 \times 10^5$, and 1.92×10^5 ($U_\infty = 10$, 15, and 20 m/s, respectively), where ν is the kinematic viscosity.

The induced velocity generated by the plasma actuator is measured using a Pitot-static probe (United Sensor) whose sensing stem diameter is $1/16''$ connected to a digital manometer (MKS 220D) having the measurement range of $0 - 1$ torr and the maximum uncertainty of 0.15%. When the plasma actuator operates at 10 $\mathrm{kV_{p-p}}$, the closest distance that the probe tip can reach is about 4 mm from the wire electrode, otherwise a high voltage arc occurs, leading to a dielectric layer break. Therefore, for safety, the measurement is conducted at 5 mm downstream from the wire electrode and 1 mm above the dielectric layer.

The voltage and frequency applied to the plasma actuator are measured with a digital oscilloscope (Keysight DSOX4104A) of 1 GHz bandwidth and a $\times$1000 high voltage (HV) probe (Tektronics P6015A) (figure 2.3). The power dissipated by the plasma actuator is measured by means of a monitor capacitor installed between the encapsulated electrode and ground (Ashpis *et al.* 2012). By simultaneously measuring the voltages across the actuator and the monitor capacitor, the dissipated energy per

cycle can be obtained by calculating the area enclosed by the Lissajous figure plotted with regard to the two voltages. Consequently, the dissipated power per unit actuator length (P_d) is given as

$$P_\mathrm{d} = \frac{fC_\mathrm{m}}{l} \oint V_\mathrm{a} \mathrm{d}V_\mathrm{m}, \tag{2.1}$$

where f is the driving frequency, and C_m and V_m are the capacitance (11 nF) and voltage across the monitor capacitor, respectively.

The drag on the vehicle model is measured using a one-axis load cell (AND LCB03K003M) whose measurement range is $0 - 3$ kgf and maximum uncertainty is 0.02%. The output from the load cell is amplified and sampled for 45 s at a rate of 10 kHz to obtain a fully converged mean drag. The data from the measurement are transferred to a computer through an A/D converter (NI PCI-6251), after which they are post-processed. All the measurements are conducted with at least two independent runs. The drag coefficient (C_D) is defined as

$$C_D = \frac{D}{\frac{1}{2}\rho U_\infty^2 A_\mathrm{f}}, \tag{2.2}$$

where D is the time-averaged drag, ρ is the air density, and A_f is the frontal area (including the stilts) of the vehicle model.

To measure the surface pressure on the slanted and vertical base surfaces of the model, 48 pressure taps are installed (36 and 12 on the slanted and vertical base surfaces, respectively). The pressure taps are connected to a digital manometer (MKS 220D) having the measurement range of $0 - 1$ torr and the maximum uncertainty of 0.15%. At each measurement point, the pressure is measured for 30 s to obtain a fully converged mean value. The signals from the manometer are sampled at the rate of 10 kHz and transferred to a computer through an A/D converter (NI PCI-6251).

The pressure coefficient (C_P) is defined as

$$C_P = \frac{P - P_\infty}{\frac{1}{2}\rho U_\infty^2}, \tag{2.3}$$

where P is the surface pressure, and P_∞ is the static pressure at the free-stream. Note that all the measurements above are conducted with shielded cables to avoid any electromagnetic noise during signal acquisitions.

The velocity fields near the slanted and vertical base surfaces of the model are measured using a particle image velocimetry (PIV). Our PIV system consists of a fog generator (SAFEX), a double-pulsed Nd:YAG laser (Litron Lasers) operating at 145 mJ − 15 Hz, a CCD camera (Vieworks VH-4M) with a 2048×2048 pixel^2 resolution, and a timing hub (Integrated Design Tools). The fog generator produces liquid droplets of approximately 1 μm in diameter that are introduced into the wind tunnel. The laser illuminates the plane of interest with a 532 nm light sheet. The delay between two pulses is generated by the timing hub. The schematic diagram of the planes of interest for the PIV measurement is given in figure 2.4. Two (x, y) planes at $z/Z = 0$ and -0.325 are considered for the measurement, where (x, y, z) = (0, 0, 0) corresponds to the lower center locations of the vertical base. An iterative cross-correlation analysis is employed with an initial interrogation window size of 64×64 pixel^2 to obtain a final window size of 16×16 pixel^2 with an overlapping by 25%. The resultant spatial resolution is $0.0152H$. To obtain a fully converged mean velocity field, 2000 instantaneous fields are taken and averaged at each plane.

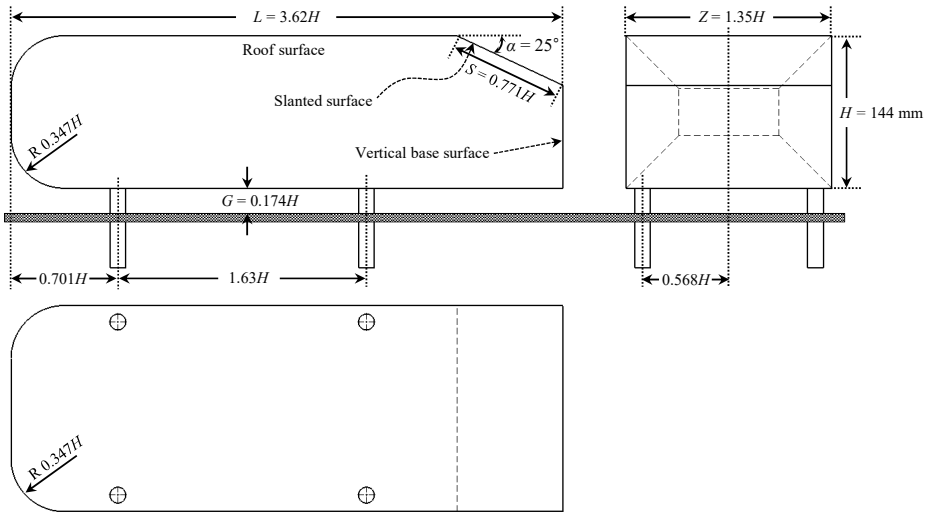

FIGURE 2.1. Schematic diagram of the Ahmed body (redrawn from Ahmed *et al.* 1984).

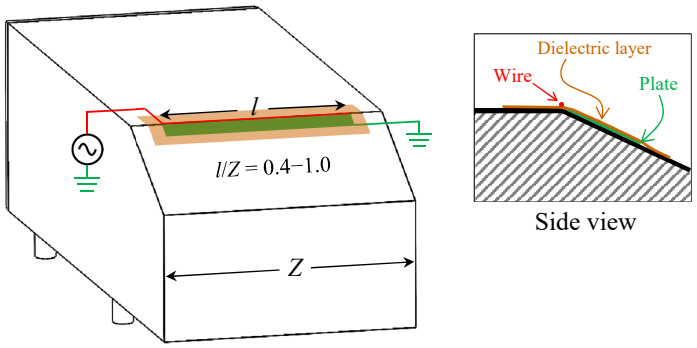

FIGURE 2.2. Wire-to-plate plasma actuator attached on the Ahmed body. Here l is the actuator length.

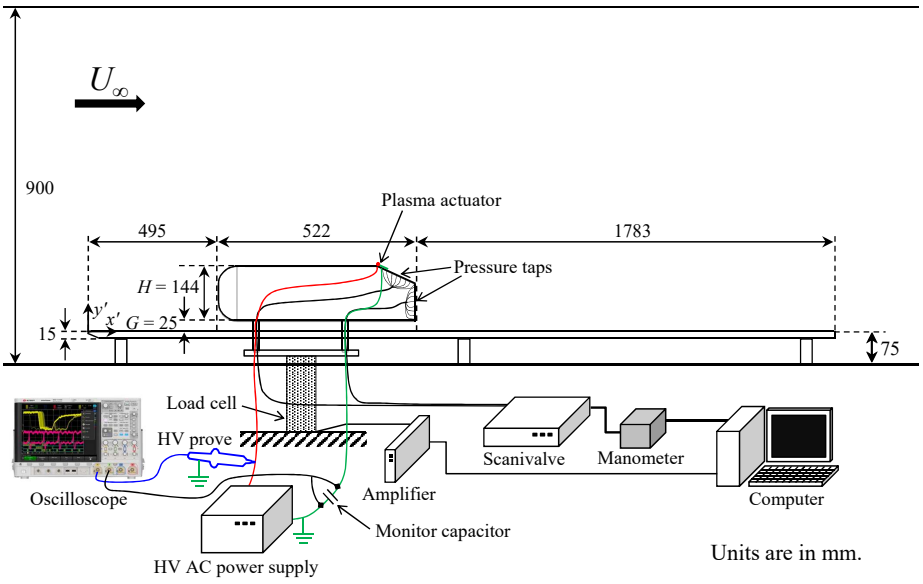

FIGURE 2.3. Schematic diagram of the experimental setup for the drag, surface-pressure and voltage measurements.

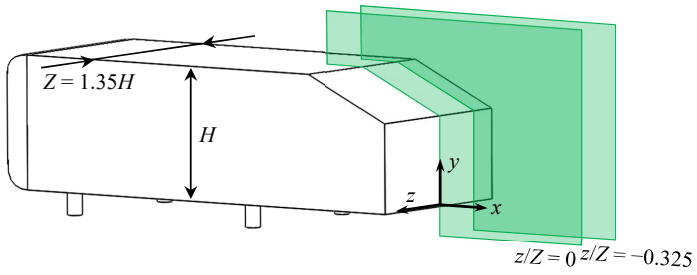

FIGURE 2.4. Planes of interest for the PIV measurement.

Chapter 3

Results

3.1. Characteristics of the plasma actuator

We investigate the induced velocity and power consumption by the present plasma actuator. Figure 3.1 shows the mean velocity induced by the wire-to-plate actuator together with that by a conventional plate-to-plate actuator. For the wire-to-plate actuator, the induced velocity is almost linearly proportional to the applied voltage for $V_\mathrm{a} \leqslant 9\ \mathrm{kV_{p-p}}$, and is significantly higher than that of the plate-to-plate actuator. Its maximum induced velocity is 4.2 m/s at $V_\mathrm{a} = 9\ \mathrm{kV_{p-p}}$. It is notable that the induced velocity slightly diminishes at $V_\mathrm{a} = 10\ \mathrm{kV_{p-p}}$, which is probably due to random glowed streaks emerging at this voltage level that weaken the plasma density outside themselves owing to their relatively high conductivity (Pouryoussefi *et al.* 2015; Shadmani *et al.* 2018).

Figure 3.2 shows the variations of the dissipated power per unit length with the applied voltage for the wire-to-plate and plate-to-plate actuators. As the applied voltage increases, the power dissipation of the wire-to-plate actuator increases fitting to the power of 3.13. However, the plate-to-plate actuator increases the power consumption more rapidly with increasing applied voltage, fitting to the power of 3.84. Consequently, the power dissipation of the wire-to-plate actuator is less than that of the plate-to-plate actuator, reaching about 50% reduction at $V_\mathrm{a} = 9\ \mathrm{kV_{p-p}}$ under the present setup. The reason for this reduction is an inhibition of filamentary

microdischarges, which dissipate a substantial amount of electric power, by using a thin wire as the exposed electrode (Hoskinson & Hershkowitz 2010; Debien *et al.* 2012*b*).

3.2. Drag variation

Figure 3.3 shows the variations of the drag reduction rate, $\Delta D = 100\times(D_{\mathrm{base}}-D_{\mathrm{control}})/D_{\mathrm{base}}$, on the Ahmed body with the applied voltage and the electrode length for the wire-to-plate and plate-to-plate actuators at three different Reynolds numbers ($Re_H = 0.96\times10^5, 1.44\times10^5$, and 1.92×10^5). At $Re_H = 0.96\times10^5$, the drag reduction rate increases with increasing applied voltage, reaches maximum at $V_{\mathrm{a}} = 9-10$ $\mathrm{kV_{p-p}}$, and then saturates or even slightly decreases at higher applied voltages. This is probably due to the onset of the glowed streaks appearing along the exposed electrode mentioned in the previous section. The drag reduction rate increases with increasing actuator length for $l/Z \leqslant 0.8$, and maximum drag reduction of about 10% occurs at $l/Z = 0.8$ and $V_{\mathrm{a}} = 9$ $\mathrm{kV_{p-p}}$ (figure 3.3(a)). This maximum value is higher than those by the present plate-to-plate actuator (8.2%) and by the plate-to-plate actuators in the previous studies. For example, Boucinha *et al.* (2011) obtained 7.9% drag reduction at $V_{\mathrm{a}} = 26$ $\mathrm{kV_{p-p}}$ and $f = 1$ kHz with a similar actuator length. Shadmani *et al.* (2018) reported 7.3% drag reduction at $V_{\mathrm{a}} = 6$ $\mathrm{kV_{p-p}}$ and $f = 10$ kHz with an actuator of $l/Z = 1.0$. It is notable that the present drag reduction rates at $l/Z = 1.0$ and $V_{\mathrm{a}} \geqslant 7$ $\mathrm{kV_{p-p}}$ are smaller than those at $l/Z = 0.8$, which may indicate that the streamwise momentum forcing by the plasma actuator at the lateral sides has a detrimental effect on the flow above the slanted surface. At higher Reynolds numbers of $Re_H = 1.44\times10^5$ and 1.92×10^5, the changes in the drag reduc-

tion rate with the length of the actuator are much smaller than those at $Re_H = 0.96 \times 10^5$. Nevertheless, the behaviors of ΔD with l and V_a are still similar to those at $Re_H = 0.96 \times 10^5$ (figures 3.3(b) and (c)). The maximum ΔD's at $Re_H = 1.44 \times 10^5$ and 1.92×10^5 are 6.8% and 2.7%, respectively.

Figure 3.4 shows the variations of the control efficiency ($\eta = (D_\mathrm{base} - D_\mathrm{control})U_\infty / lP_\mathrm{d}$), defined as the ratio of the power reduction to the dissipated power, with the applied voltage and actuator length. The efficiencies with the wire-to-plate actuator are much higher than those with the plate-to-plate actuator. This significant improvement is attributed to the reduction of the power consumption (figure 3.2) and the enhancement of the drag reduction (figure 3.3). At $Re_H = 0.96 \times 10^5$, the efficiency decreases with increasing applied voltage because of relatively small amounts of saved power by drag reduction at this level of free-stream velocity but large power consumption at high voltages (figure 3.2). At higher Re_H's, with the wire-to-plate actuator, the efficiency increases with V_a and its maximum occurs at $V_\mathrm{a} = 7-8\ \mathrm{kV_{p-p}}$. The efficiencies are higher at $V_\mathrm{a} \geqslant 7\ \mathrm{kV_{p-p}}$ than those at $Re_H = 0.96 \times 10^5$. This is because the saved power ($\Delta D \cdot D_\mathrm{base} U_\infty / 100$) increases as U_∞^3 ($D_\mathrm{base} \sim U_\infty^2$) with increasing Re_H, although ΔD's at high Re_H's are still lower than those at $Re_H = 0.96 \times 10^5$. Since the dissipated power per unit length of the actuator increases as $V_\mathrm{a}^{3.13}$ (figure 3.2), the most efficient actuator length obtained is $l/Z = 0.5$ (figure 3.4).

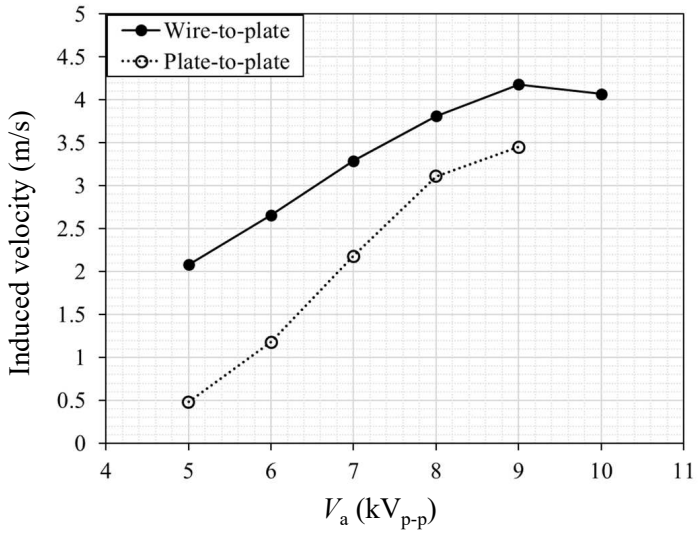

FIGURE 3.1. Variations of the mean velocity induced by the wire-to-plate and plate-to-plate plasma actuators with the applied voltage (measured at 5 mm downstream from the wire electrode and 1 mm above the dielectric layer).

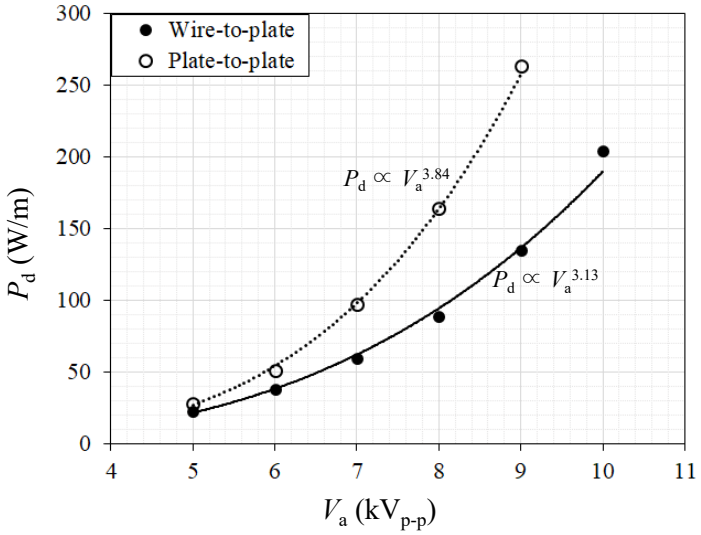

FIGURE 3.2. Variations of the mean dissipated power per unit length of the wire-to-plate and plate-to-plate plasma actuators with the applied voltage.

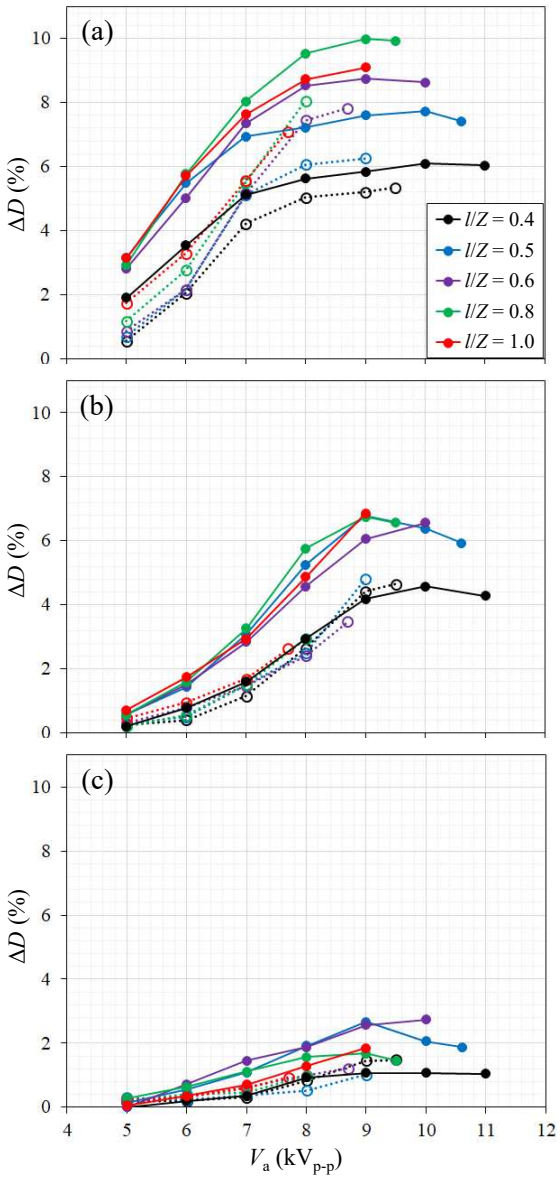

FIGURE 3.3. Variations of the drag reduction rate (ΔD) with the applied voltage and actuator length by the wire-to-plate (solid lines with solid symbols) and plate-to-plate (dotted lines with open symbols) actuators: (a) $Re_H = 0.96 \times 10^5$; (b) 1.44×10^5; (c) 1.92×10^5.

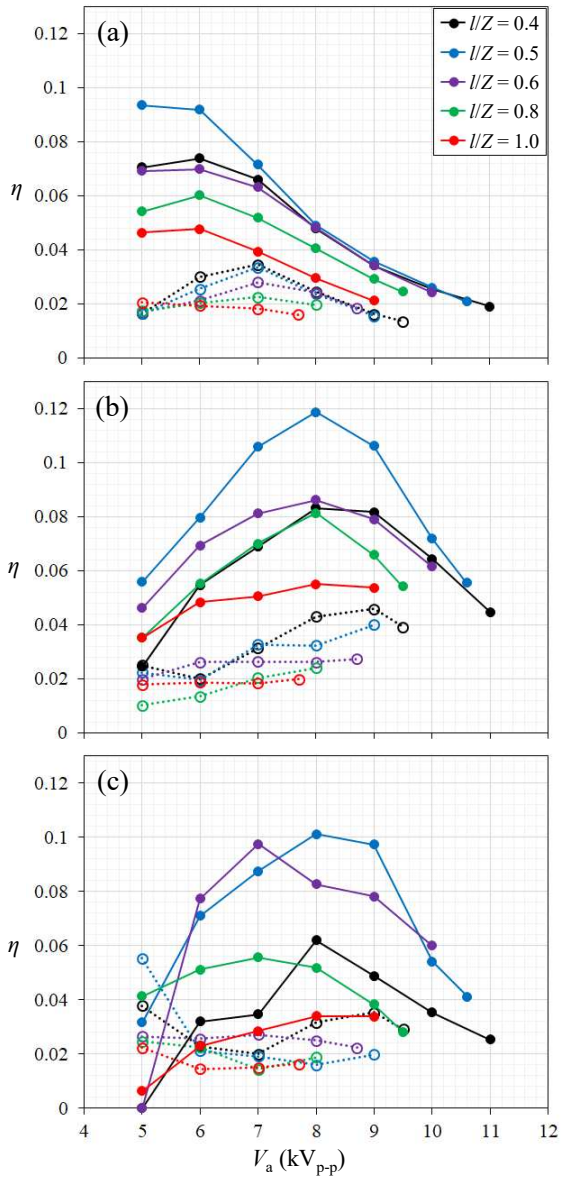

FIGURE 3.4. Variations of the control efficiency with the applied voltage and actuator length by the wire-to-plate (solid lines with solid symbols) and plate–to-plate (dotted lines with open symbols) actuators: (a) $Re_H = 0.96 \times 10^5$; (b) 1.44×10^5; (c) 1.92×10^5.

Chapter 4

Discussions

4.1. Flow modifications for the case of largest drag reduction rate

The case of $l/Z = 0.8$ and $V_{\mathrm{a}} = 9\ \mathrm{kV_{p-p}}$ at $Re_H = 0.96 \times 10^5$ provided the largest drag reduction rate of 10%. Thus, we investigate the mechanism responsible for the largest drag reduction by analyzing the flow fields near and surface pressures on the slanted and vertical base surfaces. Figure 4.1 shows the changes in the mean streamlines and streamwise velocity by the plasma actuator of $l/Z = 0.8$ at the center and off-center planes. Without actuation, the flow separates at the front edge of the slanted surface, forming a separation bubble there. With the actuation, the flow above the slanted surface is attached at both spanwise locations by the streamwise momentum induced by the actuation. Accordingly, the surface pressure at $|z/Z| < 0.4$ (except both corners) is significantly recovered (see figures 4.2(a) and (c)). Also, the main separation bubble behind the vertical surface locates farther downstream, and thus the pressure on the vertical base surface is increased, also contributing to the drag reduction. We compute the surface pressure difference between the cases with and without actuation and find that about 70% of the total drag reduction comes from the pressure recovery on the slanted surface.

4.2. Effect of the actuator length on the flow field

We consider three different actuator lengths ($l/Z = 0.5$, highest efficiency; 0.8, largest drag reduction; 1.0) and investigate its effect on the flow field. Due to the flow separation at the front edge of the slanted surface without actuation, the pressure coefficient is negative there, increases downstream, and is nearly constant on the base surface (figure 4.2(a)). With the actuator of $l/Z = 0.5$ (figure 4.2(b)), the streamwise momentum induced delays the separation at $|z/Z| < 0.25$ (see below), and the pressure significantly recovers at $|z/Z| < 0.4$ and on the base surface (except at $|z/Z| > 0.25$ and $s/S > 0.8$ where the pressure coefficient is even lower than that of no actuation, possibly due to the shear-layer interaction between the flows with and without actuation (Pope 2000)). With the actuator of $l/Z = 0.8$ (figure 4.2(c)), the front edge separation nearly disappears (see below) and thus the pressure recovers at $|z/Z| < 0.4$ on the slanted and vertical base surfaces. The pressure recovery at $|z/Z| < 0.4$ with $l/Z = 0.8$ is even more than that with $l/Z = 0.5$ (figures 4.2(b) and (c)). With $l/Z = 1.0$ (figure 4.2(d)), the pressure distribution is not different from that with $l/Z = 0.8$, suggesting that the actuation at the lateral sides of the front edge is not effective, possibly due to the existence of the longitudinal vortices there.

Figure 4.3 shows the mean streamlines and contours of the Reynolds shear stress near the slanted and vertical base surfaces with and without actuation. Without actuation, the Reynolds shear stress is large above the slanted surface due to shear layer above the separation bubble. This large Reynolds shear stress nearly disappears with the actuator of $l/Z = 0.8$ due to the separation delay. With $l/Z = 0.5$, the Reynolds shear stress is not small near the front edge of the slanted surface at an off-center plane

($z/Z = -0.325$) because of the small separation bubble there.

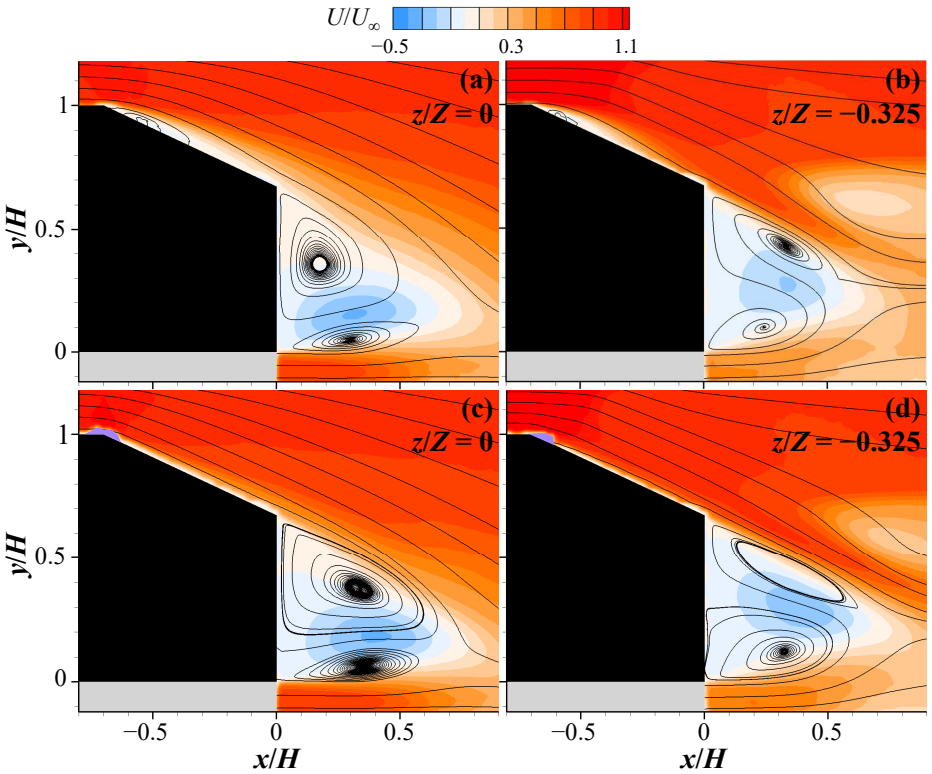

FIGURE 4.1. Mean streamlines and contours of the mean streamwise velocity ($Re_H = 0.96 \times 10^5$): (a, b) without and (c, d) with the actuation ($l/Z = 0.8$ and $V_\mathrm{a} = 9$ $\mathrm{kV_{p-p}}$). The purple areas at the front edge of the slanted surface in (c) and (d) could not be measured due to the light emission from the plasma actuator.

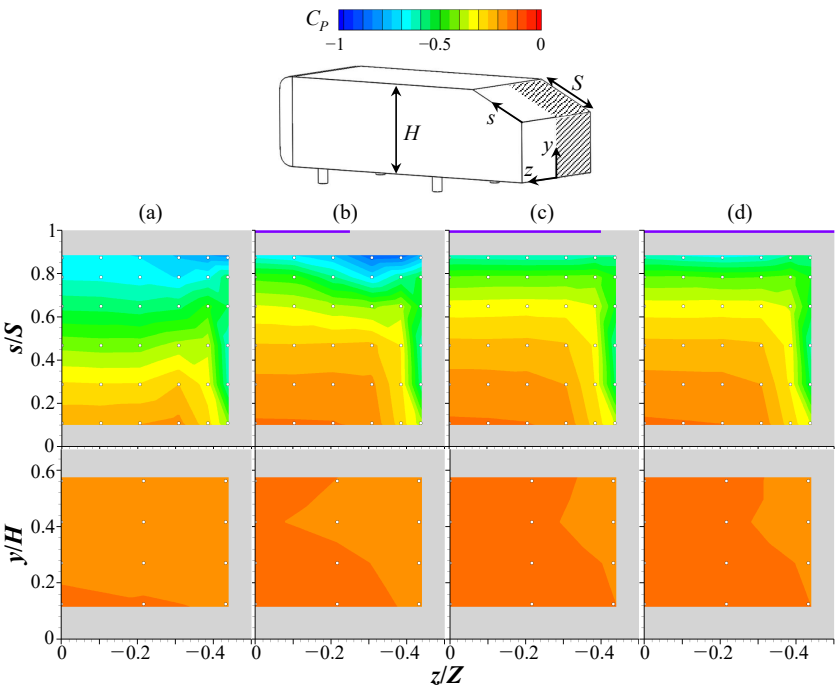

FIGURE 4.2. Contours of the mean pressure coefficient on the slanted and vertical base surfaces ($Re_H = 0.96 \times 10^5$): (a) without actuator; (b) with the actuator of $l/Z = 0.5$; (c) $l/Z = 0.8$; (d) $l/Z = 1.0$ ($V_\mathrm{a} = 9\ \mathrm{kV_{p-p}}$). White circles in this figure denote the locations of the pressure measurement.

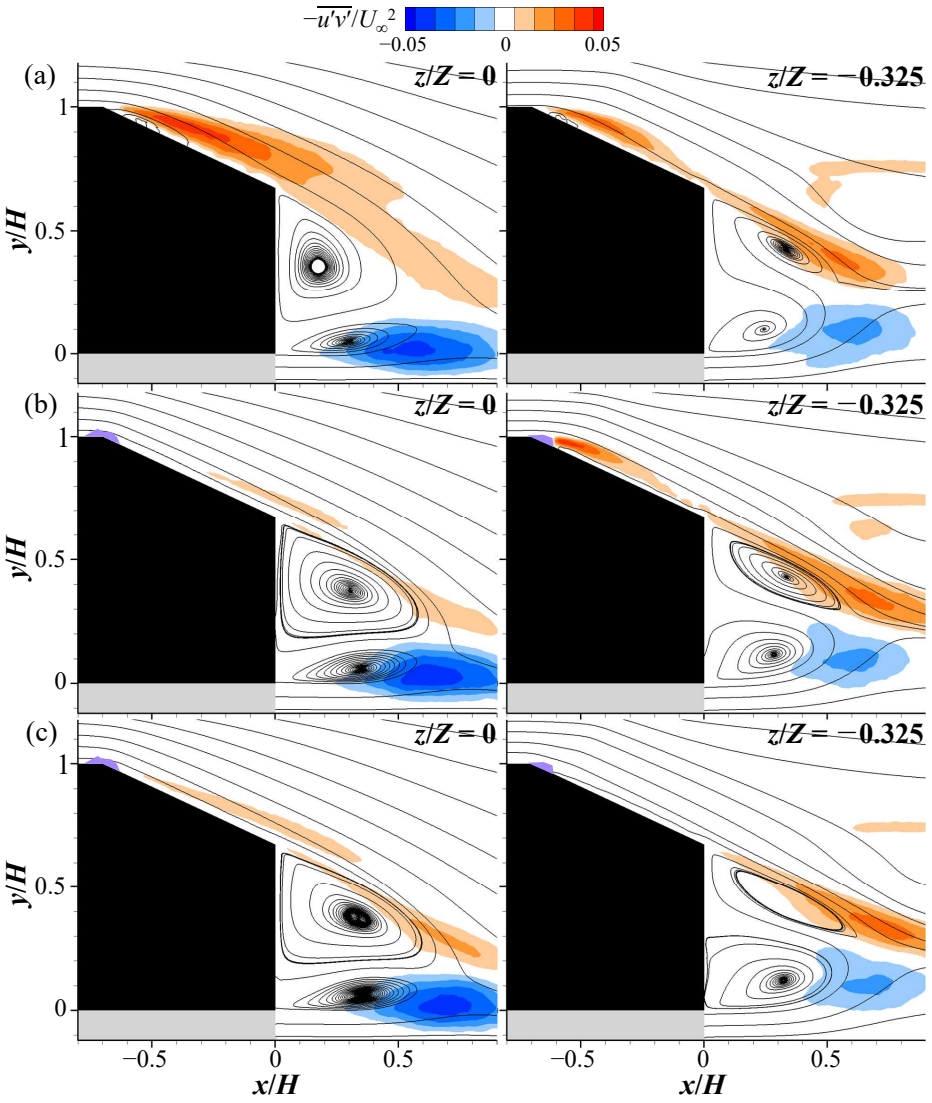

FIGURE 4.3. Mean streamlines and contours of the Reynolds shear stress ($-\overline{u'v'}$) ($Re_H = 0.96 \times 10^5$): (a) without actuator; (b) with the actuator of $l/Z = 0.5$; (c) $l/Z = 0.8$ ($V_\mathrm{a} = 9$ $\mathrm{kV_{p-p}}$). The purple areas at the front edge of the slanted surface in (b) and (c) could not be measured due to the light emission from the plasma actuator.

Chapter 5

Further drag reduction at high Re_H employing a sawtooth-shaped electrode

Although the performance and efficiency of the plasma actuator are significantly enhanced by employing the wire-to-plate configuration, its performance is still limited at the high Re_H of 1.92×10^5 mainly due to the relatively low induced velocity compared to the free-stream velocity. Since the induced velocity by the present plasma actuator is saturated to about 4.2 m/s at $V_\mathrm{a} \geqslant 9$ $\mathrm{kV_{p-p}}$ (figure 3.1), another mechanism rather than a two-dimensional momentum forcing in the boundary layer is required for further drag reduction at the high Re_H. Therefore, in this chapter, we introduce a plasma actuator with a sawtooth-shaped exposed electrode (or a sawtooth plasma actuator) that can generate three-dimensional momentum forcing owing to its geometry (Joussot *et al.* 2013; Liu *et al.* 2016; Wang *et al.* 2017), and compare its effect with that of the linear wire-to-plate and plate-to-plate actuators. The sawtooth-shaped electrode is made of copper tape, and two different sawtooth geometries having the width (λ) to height (h) ratio of 1.2 and 2 are considered (figure 5.1). The sawtooth plasma actuators are installed at the edge between the roof and slanted surface such that the tips of the exposed electrode locate at this edge. Their lengths are fixed to $0.8Z$, with which the drag reduction rate was the largest for the linear actuators (figure 3.3), so that the electrodes of $\lambda/h = 1.2$ and $\lambda/h = 2$ have 20 and 12 teeth in total, respectively.

5.1. Characteristics of the sawtooth plasma actuator

We investigate the induced velocity and power consumption by the sawtooth and linear plasma actuators. Figure 5.2 shows the variations of mean velocity induced by the sawtooth actuators with the applied voltage and spanwise location, together with those by the linear actuators. With the sawtooth actuator of $\lambda/h = 1.2$, the velocity profiles do not show a clear trend along the span at $V_\mathrm{a} \leqslant 7$ $\mathrm{kV_{p-p}}$, but there appear local peaks near the roots and tips at $V_\mathrm{a} \geqslant 8$ $\mathrm{kV_{p-p}}$. The peaks near the roots are probably due to the accumulation of the induced flow diverged from the tips caused by the electrode geometry (Joussot *et al.* 2013; Liu *et al.* 2016). Nevertheless, the peak induced velocities are lower than the induced velocities by the linear plate-to-plate actuator at the same applied voltages. On the other hand, with $\lambda/h = 2$, the velocity profiles show a clear trend at all the applied voltages, and the peaks only appear near the tips possibly due to larger intervals between the them. The peak induced velocities with $\lambda/h = 2$ are comparable with the induced velocities by the plate-to-plate actuator, but are still lower than those by the wire-to-plate actuator at the same applied voltages.

Figure 5.3 shows the variations of the dissipated power ($P_\mathrm{D} = lP_\mathrm{d}$) with the applied voltage for the sawtooth and linear actuators. It is remarkable that the power dissipations of the sawtooth actuators are even smaller than that of the wire-to-plate actuator at the same applied voltage since the actuation occurs near the tips only, for which the actuator of $\lambda/h = 1.2$ dissipates more power than that of $\lambda/h = 2$. Nevertheless, the rate of additional power reduction by the sawtooth actuators ($1 - P_{\mathrm{D_{sawtooth}}}/P_{\mathrm{D_{linear}}}$) decrease as the applied voltage increases because the power dissipations of them fit to the power of more than 4.4, while

those of the linear actuators fit to the power of less than 3.9.

5.2. Drag variation

Figure 5.4 shows the variations of the drag reduction rate (ΔD) with the applied voltage for the sawtooth and linear actuators at three different Reynolds numbers ($Re_H = 0.96 \times 10^5, 1.44 \times 10^5$, and 1.92×10^5). At $Re_H = 0.96 \times 10^5$, ΔD by the sawtooth actuator of $\lambda/h = 1.2$ is larger than those by the linear actuators at $V_\mathrm{a} \leqslant 7$ $\mathrm{kV_{p-p}}$. However, it becomes saturated at $V_\mathrm{a} > 7$ $\mathrm{kV_{p-p}}$, so that ΔD by the wire-to-plate actuator becomes larger than that by the sawtooth actuator of $\lambda/h = 1.2$. ΔD by the sawtooth actuator of $\lambda/h = 2$ is smaller than that by the sawtooth actuator of $\lambda/h = 1.2$ probably due to fewer teeth, i.e. fewer actuation points. At higher Re_H of 1.44×10^5 and 1.92×10^5, it is notable that ΔD's of the sawtooth actuators are not very different from those at $Re_H = 0.96 \times 10^5$, whereas those by the linear actuators decrease significantly, even though the induced velocities by the sawtooth actuators are lower than those by the linear actuators at $V_\mathrm{a} \geqslant 6$ $\mathrm{kV_{p-p}}$ (figure 5.2). This suggests that, unlike the two-dimensional momentum forcing, the three-dimensional momentum forcing on the flow above the slanted surface is effective even at the high Re_H, reaching 8.2% of drag reduction at $Re_H = 1.92 \times 10^5$.

Figure 5.5 shows the variations of the control efficiency (η) with the applied voltage for the sawtooth and linear actuators. The efficiencies with the sawtooth actuators are substantially higher than those with the linear actuators, reaching the maximum efficiency of about 0.56 at $Re_H = 1.92 \times 10^5$ with $\lambda/h = 1.2$. This significant improvement is attributed to the reduction of the power consumption (figure 5.3) and the enhancement

of the drag reduction (figure 5.4). The behaviors of the efficiencies with the sawtooth actuators with increasing the applied voltage are similar to those with the wire-to-plate actuator (see section 3.2).

5.3. Flow modifications

The sawtooth actuator of $\lambda/h = 1.2$ provided the drag reduction rate of more than 8% at $V_{\mathrm{a}} = 9$ $\mathrm{kV_{p-p}}$ and $Re_H = 1.92 \times 10^5$, which is significantly higher than that by the linear actuators. Thus, we investigate the mechanism responsible for the large drag reduction at the high Re_H by analyzing the flow fields near and surface pressures on the slanted and vertical base surfaces. Figure 5.6 shows the changes in the mean streamlines and streamwise velocity by the wire-to-plate actuator and sawtooth actuator of $\lambda/h = 1.2$ at the center plane ($l/Z = 0.8$). Without the actuation, the flow topology near the slanted and vertical base surfaces is similar to that at $Re_H = 0.96 \times 10^5$, with the main and secondary separation bubbles (figures 4.1(a) and 5.6(a)). With the actuation by the wire-to-plate actuator, the size of the secondary separation bubble on the slanted surface is slightly reduced, but the overall shape of the wake remains similar to that without actuation. Accordingly, the surface pressure is slightly recovered near the actuator at $s/S > 0.8$, but otherwise it is not different from that without actuation (see figures 5.7(a) and (b)). On the other hand, with the actuation by the sawtooth actuator, the separated flow is nearly attached on the slanted surface (figures 5.6(c) and (d)), so that the pressure on the slanted surface is significantly recovered, except near its front edge (figures 5.7(a) and (c)). We found no meaningful difference between the flows above the slanted surface at the root- and tip-planes. Meanwhile, the main separation bubble behind the vertical

base surface moves downstream, and thus the pressure on the vertical base surface is increased, also contributing to the drag reduction.

Figure 5.8 shows the contours of the Reynolds shear stress near the actuator on the slanted surface without and with the actuation by the wire-to-plate actuator and sawtooth actuator of $\lambda/h = 1.2$. With the linear wire-to-plate actuator, the Reynolds shear stress above the slanted surface little changes. On the other hand, with the sawtooth actuator, there occurs a high stress region very near the actuator, and then it decays downstream. For the present sawtooth actuator, the plasma formation is concentrated near its tips, so that the characteristics of the flows induced there should be inherently similar to that of the flow induced near the ends of the linear actuator because both flows are induced near sharp edges of the exposed electrode (see section 4.2). Hence, the flow induced by the sawtooth actuator can induce a faster development of the shear layer, due to the shear-layer interaction between the flows with and without actuation near the tips. Consequently, the momentum mixing inside the boundary layer is significantly enhanced so that the separated flow can be attached onto the surface despite of high free-stream velocity (figure 5.6(c) and (d)). Also, it is found that the shear-layer interaction at the root-plane is stronger than that at the tip-plane, which is possibly due to the high velocity fluctuation caused by the collision between the flows induced from the adjacent tips.

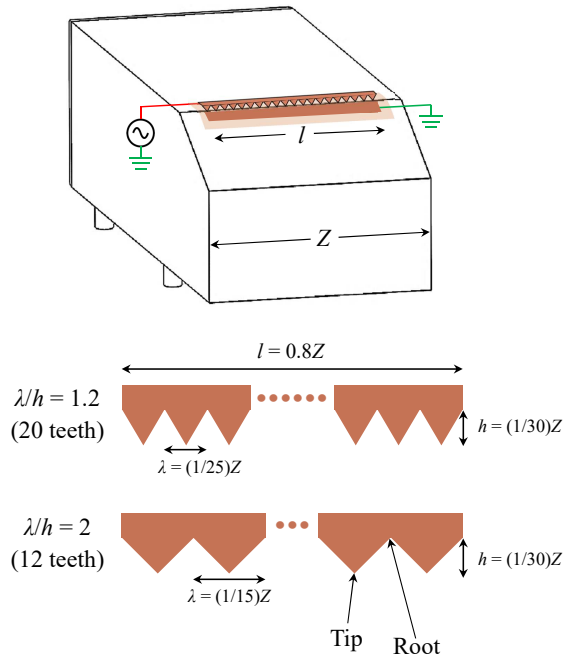

FIGURE 5.1. Sawtooth plasma actuator attached on the Ahmed body and the geometric configurations of its exposed electrode.

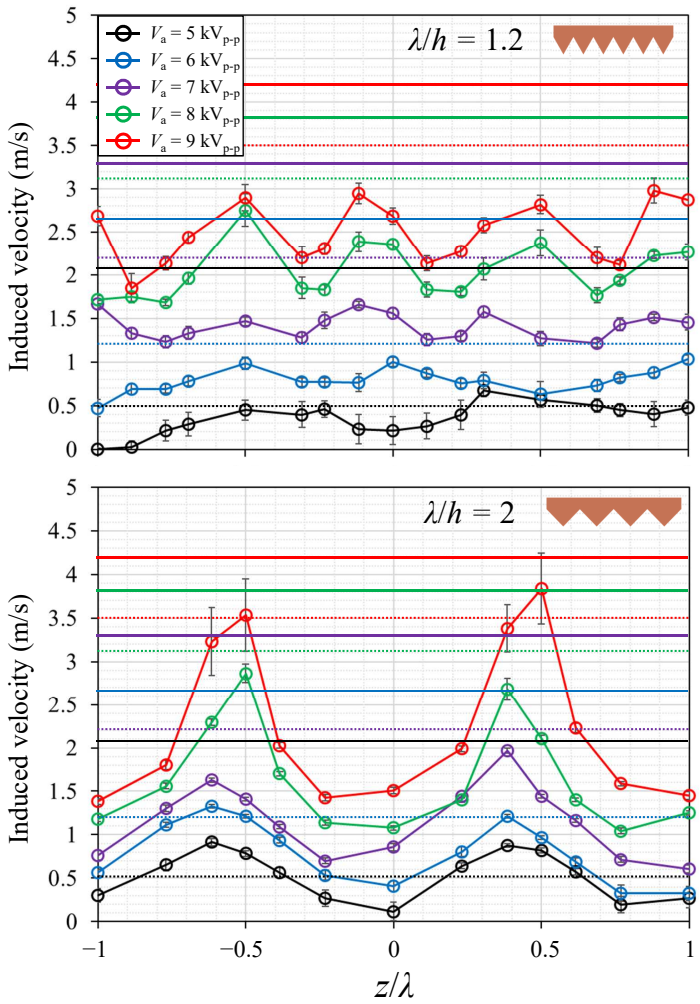

FIGURE 5.2. Variations of the mean velocity induced by the sawtooth plasma actuators of $\lambda/h = 1.2$ and 2 with the applied voltage and spanwise location (measured at 5 mm downstream from the wire electrode and 1 mm above the dielectric layer). Here, the solid and dotted horizontal lines denote the induced velocities by the wire-to-plate and plate-to-plate actuators, respectively (from figure 3.1), and $z = 0$ is where a root is.

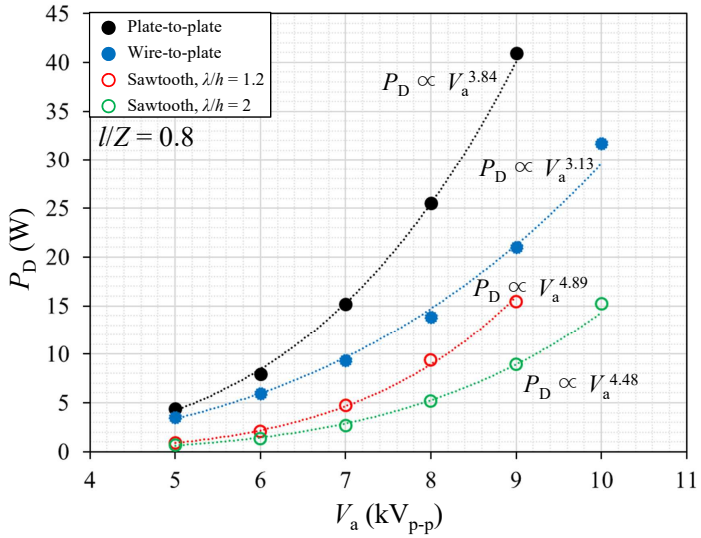

FIGURE 5.3. Variations of the mean dissipated power of the sawtooth and linear plasma actuators with the applied voltage ($l/Z = 0.8$).

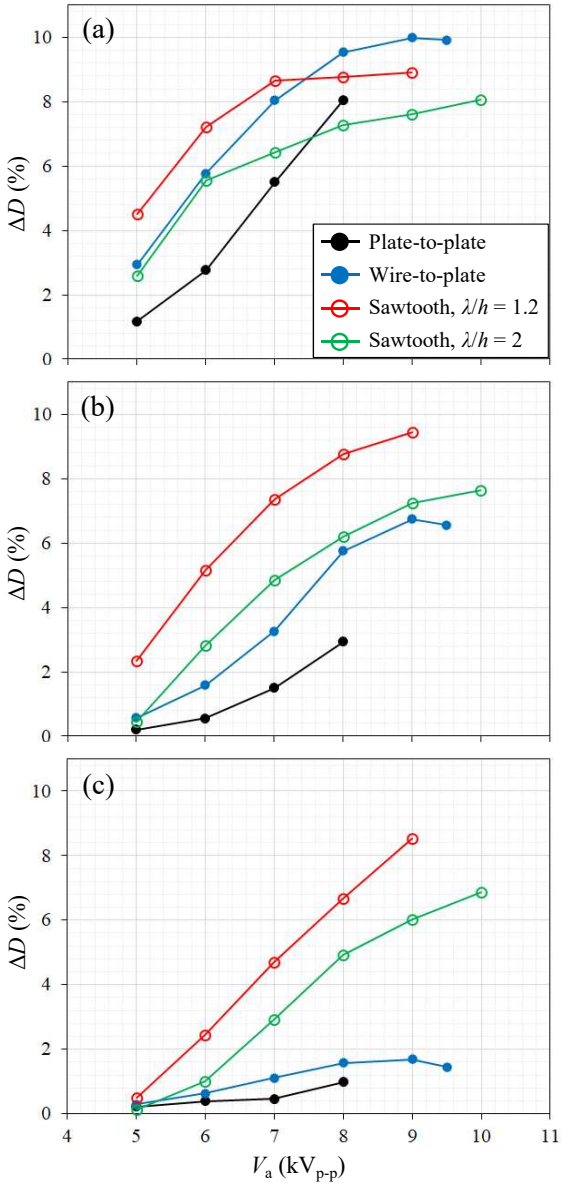

FIGURE 5.4. Variations of the drag reduction rate (ΔD) with the applied voltage by the sawtooth and linear actuators: (a) $Re_H = 0.96 \times 10^5$; (b) 1.44×10^5; (c) 1.92×10^5 ($l/Z = 0.8$).

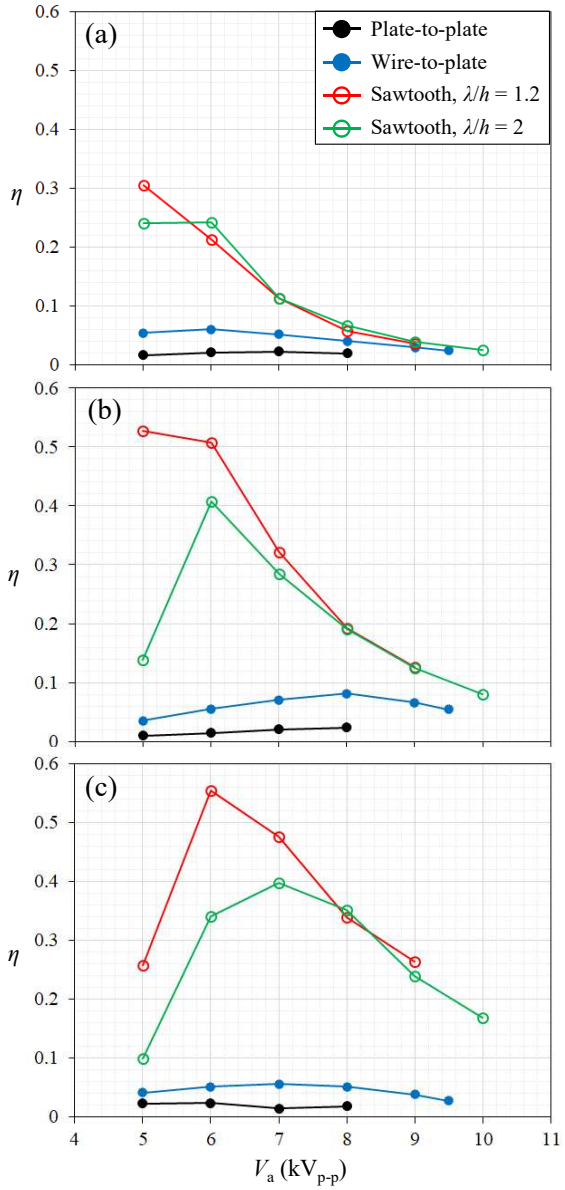

FIGURE 5.5. Variations of the control efficiency with the applied voltage by the sawtooth and linear actuators: (a) $Re_H = 0.96\times10^5$; (b) 1.44×10^5; (c) 1.92×10^5 ($l/Z = 0.8$).

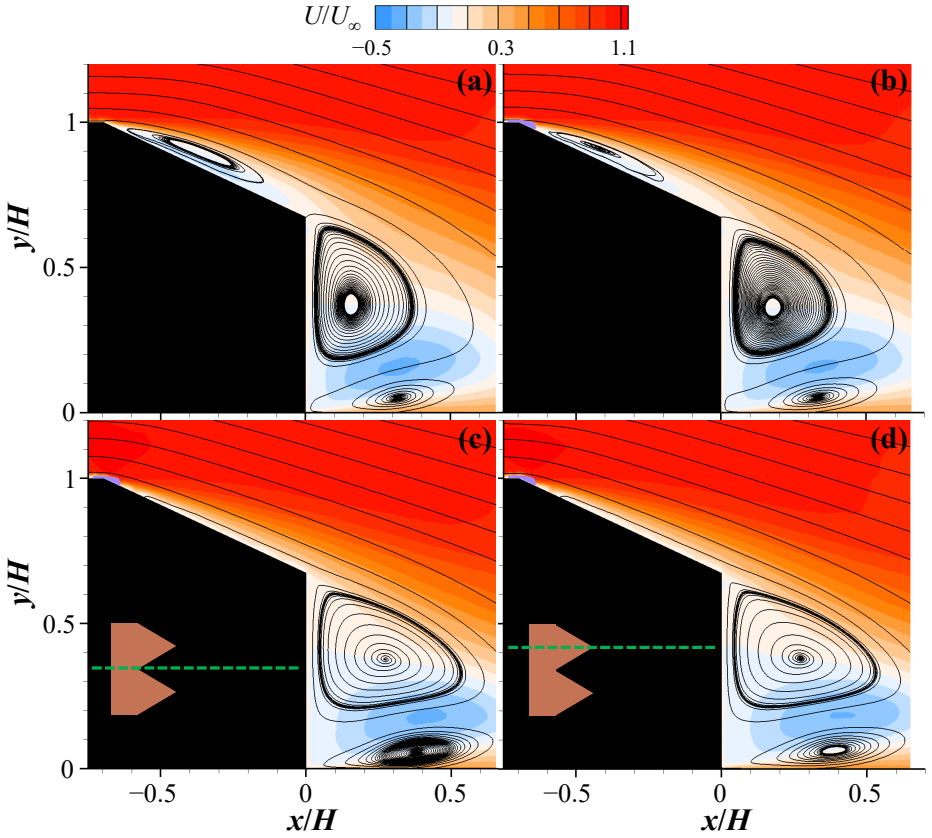

FIGURE 5.6. Mean streamlines and contours of the mean streamwise velocity ($Re_H = 1.92 \times 10^5$): (a) without and (b) with the actuation by the wire-to-plate actuator and (c, d) sawtooth actuator of $\lambda/h = 1.2$ at the root- and tip-planes, respectively ($l/Z = 0.8$ and $V_\mathrm{a} = 9$ $\mathrm{kV_{p-p}}$). Here, (a – c) and (d) are measured at $z/Z = 0$ and -0.02, respectively. The purple areas at the front edge of the slanted surface in (b – d) could not be measured due to the light emission from the plasma actuator.

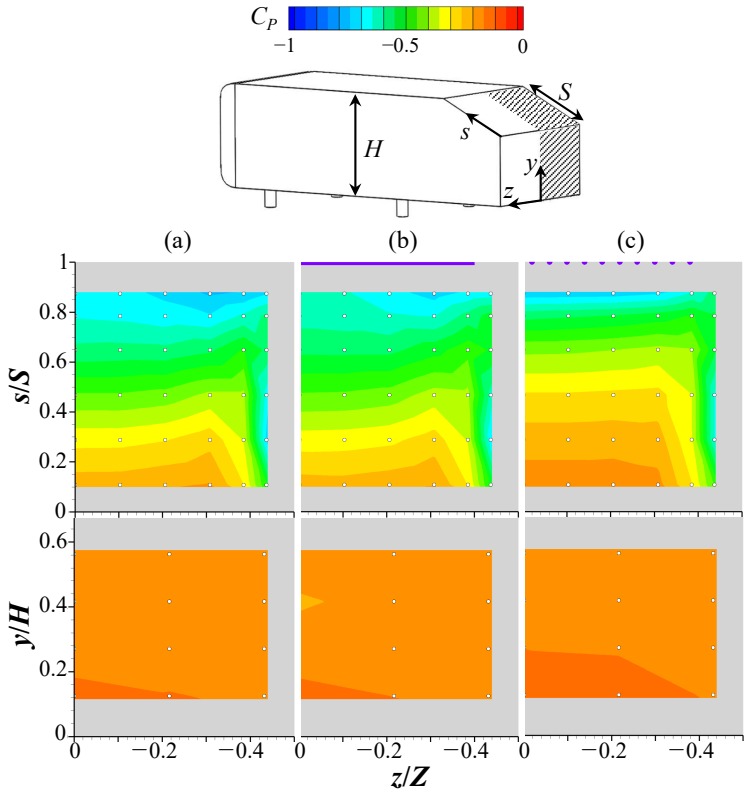

FIGURE 5.7. Contours of the mean pressure coefficient on the slanted and vertical base surfaces ($Re_H = 1.92 \times 10^5$): (a) without and (b) with the actuation by the wire-to-plate actuator and (c) sawtooth actuator of $\lambda/h = 1.2$ ($l/Z = 0.8$ and $V_{\mathrm{a}} = 9\ \mathrm{kV_{p-p}}$). White circles in this figure denote the locations of the pressure measurement.

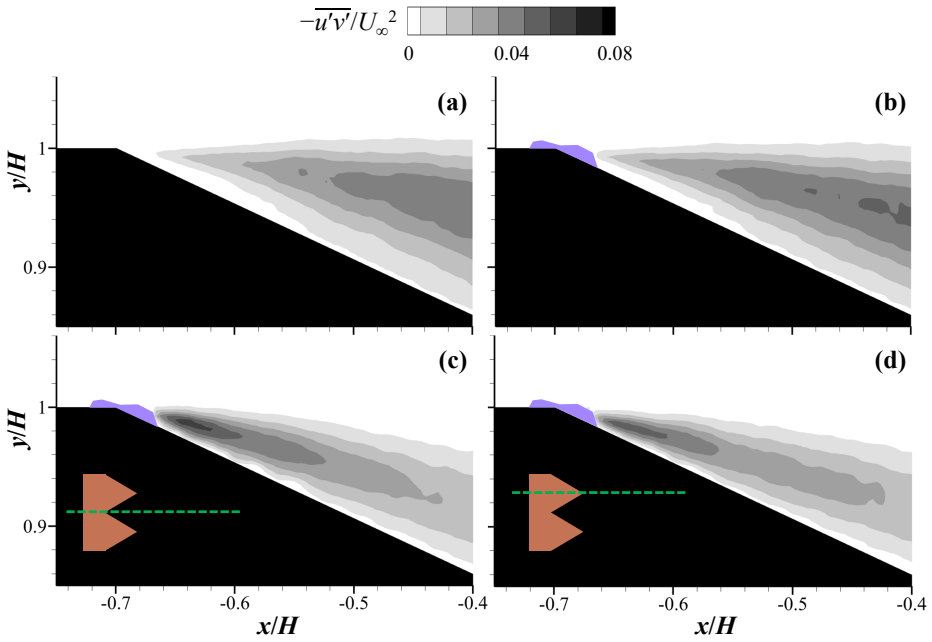

FIGURE 5.8. Mean streamlines and contours of the Reynolds shear stress ($-\overline{u'v'}$) ($Re_H = 1.92 \times 10^5$): (a) without and (b) with the actuation by the wire-to-plate actuator and (c, d) sawtooth actuator of $\lambda/h = 1.2$ at the root- and tip-planes, respectively ($l/Z = 0.8$ and $V_\mathrm{a} = 9$ $\mathrm{kV_{p-p}}$). Here, the spatial resolution is $0.00463H$, and (a – c) and (d) are measured at $z/Z = 0$ and -0.02, respectively. The purple areas at the front edge of the slanted surface in (b – d) could not be measured due to the light emission from the plasma actuator.

Chapter 6

Conclusions

In the present study, we applied a wire-to-plate DBD plasma actuator to a three-dimensional model vehicle (Ahmed body) for drag reduction. We varied the free-stream velocity, the length of plasma actuator, and the applied voltage, respectively, and measured the drag force and power consumption by the actuation. The drag reduction strongly depended on those parameters. The control performance and efficiency of the wire-to-plate actuator were better and higher than those of a conventional plate-to-plate actuator.

The maximum drag reduction rate of 10% was achieved by the actuator with $l/Z = 0.8$ at $Re_H = 0.96 \times 10^5$, and the maximum efficiency of 0.12 was achieved by the actuator with $l/Z = 0.5$ at $Re_H = 1.44 \times 10^5$. Without actuation, the flow separated at the front edge of the slanted surface, forming a separation bubble there. This flow structure induced low pressure on the slanted surface, particularly at its front edge, resulting in a high drag. However, with the actuation, the separated flow was attached onto the slanted surface because of the streamwise momentum induced by the actuation. This flow modification by the plasma actuator resulted in substantial pressure recovery on the slanted and vertical base surfaces, leading to a significant drag reduction. The effect of the actuator length on the flow field was also investigated with three different actuator lengths. With the actuator of $l/Z = 0.5$, the pressure on the center

region of the slanted surface was significantly recovered, except for the region near the actuator ends. With $l/Z = 0.8$, the front edge separation nearly disappeared, so that the pressure on the whole center region was recovered. With $l/Z = 1.0$, the pressure distribution was not different from that with $l/Z = 0.8$, suggesting that the actuation underneath the longitudinal vortices may not be so effective.

By employing a sawtooth-shaped exposed electrode, the drag reduction rate and efficiency at higher U_∞ were further enhanced, and the enhancements were higher with an actuator with larger number of teeth. With the sawtooth actuator of $\lambda/h = 1.2$, the drag reduction rate and efficiency reached up to 8.2% and 0.56, respectively, at $U_\infty = 20$ m/s. With this actuator, the development of the shear layer over the slanted surface is significantly accelerated, enhancing the momentum mixing inside the boundary layer. As a result, the momentum induced by the actuator is effectively supplied into the separated boundary layer, leading to a significant suppression of the flow separation at the front edge of the slanted surface, despite of high U_∞.

Although the present control efficiency is still less than unity in a laboratory scale experiment, the efficiency may become greater than unity when a real-scale heavy vehicle is considered, as discussed by Roy *et al.* (2016). The length scale of a heavy vehicle is at least ten times that of the present Ahmed body model. Then, at the present free-stream velocity, the drag on a real-scale vehicle, D_{base}, is increased by a hundred times that of the present one (assuming that the drag coefficient is the same), whereas the power consumption of the plasma actuator is increased by about ten times, thus increasing the efficiency by ten times for a real-scale vehicle. However, for a real-scale vehicle, the boundary layer thickness at the front

edge of the slant surface should be much larger than that of the present study. Therefore, some follow-up studies may have to be conducted to examine this conjecture. In addition, effective actuator configurations for controlling the longitudinal vortices and increasing the efficiency should be further developed. Finally, one may also consider different locations of placing the present wire-to-plate actuators in addition to the rear part of the vehicle model to obtain an additional drag reduction (see, for example, Vernet *et al.*, 2018).

Part III.

Drag reduction mechanisms by passive and active flow controls: comparison and analysis

Chapter 1

Comparative analysis of the drag reduction mechanisms by the passive and active flow control devices

In this paper, we showed that both the automatic moving deflector and DBD plasma actuator can effectively reduce the drag on the Ahmed body. It is notable that there are similarities and differences in the mechanisms responsible for the drag reductions by these two devices. Therefore, in this part, we compare and analyze in detail the drag reduction mechanisms of the AMD made of acrylic and wire-to-plate DBD plasma actuator, representatively.

By the operation of AMD, the separation point is delayed from the front edge of the slanted surface to the trailing edge of AMD, and a weak reverse flow exists in the gap between the slanted surface and AMD (figures 1.1(a) and (b)). Furthermore, the development of strong longitudinal vortices at the lateral sides of the slanted surface is significantly suppressed (figures 1.1(c) and (d)). As a result, the slanted surface is directly exposed to the flow of the wake and thus the pressure there becomes comparable to that on the vertical base surface (figures 1.2(a) and (c)). On the other hand, by the operation of the plasma actuator, the flow separation on the slanted surface is delayed to its rear edge. Nevertheless, the streamwise momentum forcing little affects the longitudinal vortices (fig-

ures 1.1(g) and (h)). As a result, the pressure on the center region of the slanted surface is significantly recovered, while it is little recovered near the lateral edge (figures 1.2(e) and (g)). Therefore, the amount of drag reduction by AMD (19%) is almost twice that by the wire-to-plate plasma actuator (10%). Meanwhile, the pressure on the vertical base surface with AMD is slightly dropped than that without AMD, whereas that with the plasma actuator is slightly recovered than that without the actuator (figures 1.2(b), (d), (f) and (h)). A pressure recovery on the base surface of a model vehicle by delaying the separation bubble is a common mechanism for the drag reduction (Choi *et al.* 2014), which can be also found in the case of the plasma actuator (figures 1.1(e) and (f)). However, it is inconsistent with the case of AMD even though the separation bubbles are delayed far downstream (figures 1.1(a) and (b)). This is because the strength of the main separation bubbles is substantially increased during their delay, resulting in a rather decrease of the pressure on the vertical base surface. A similar discussion was made by Littlewood & Passmore (2012). Consequently, the drag reduction caused by AMD is mainly from the pressure recovery on the slanted surface, while the pressure recoveries on the slanted and vertical base surfaces by the plasma actuation both contribute to the drag reduction by about 70% and 30%, respectively.

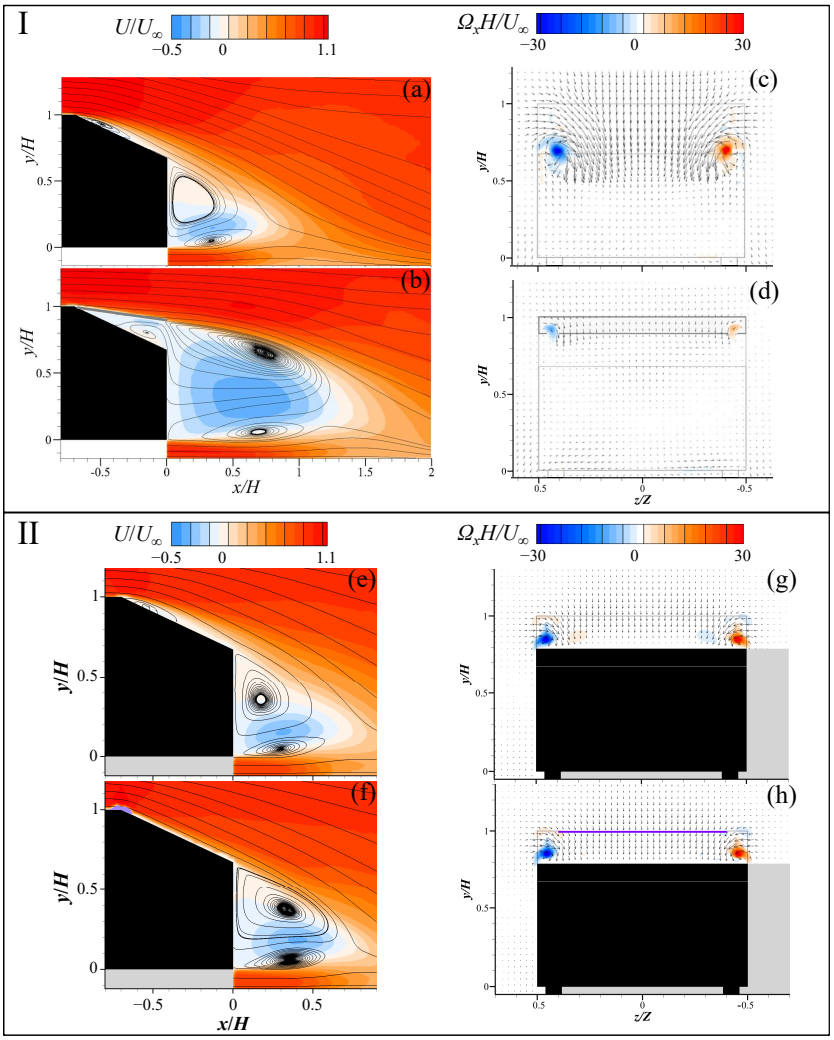

FIGURE 1.1. I. Contours of the mean streamwise velocity and the mean streamlines at (x, y) center plane and contours of the mean streamwise vorticity and the mean velocity vectors on the cross-flow plane at $x/H = 0.25$ (a, c) without and (b, d) with AMD. $Re_H = 2.9 \times 10^5$ (from figures 3.5 and 3.7 in part I). II. Contours of the mean streamwise velocity and the mean streamlines at (x, y) center plane (from figure 4.1 in part II) and contours of the mean streamwise vorticity and the mean velocity vectors on the cross-flow plane at $x/H = -0.25$ (e, g) without and (f, h) with the wire-to-plate plasma actuator. $Re_H = 0.96 \times 10^5$.

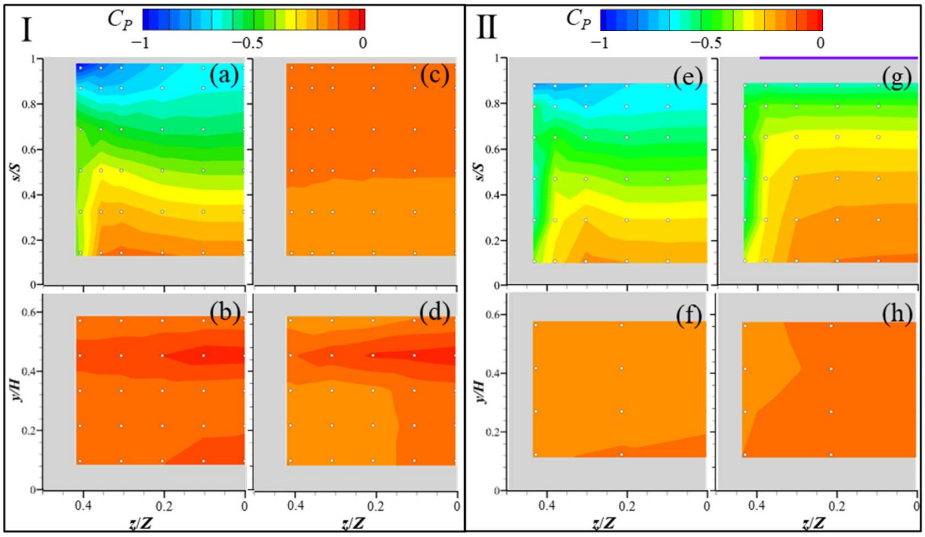

FIGURE 1.2. I. Contours of the mean pressure coefficient on the left halves of the slanted (upper) and vertical base (lower) surfaces (a, b) without and (c, d) with AMD. $Re_H = 2.9 \times 10^5$ (from figure 3.6 in part I). II. Contours of the mean pressure coefficient on the left halves of the slanted (upper) and vertical base (lower) surfaces (e, f) without and (g, h) with the wire-to-plate plasma actuator. $Re_H = 0.96 \times 10^5$ (from figure 4.2 in part II).

References

Ahmed, S. R., Ramm, G. & Faltin, G. 1984 Some salient features of the time-averaged ground vehicle wake. *SAE Technical Paper* p. 840300.

Aider, J. L., Beaudoin, J. F. & Wesfreid, J. E. 2010 Drag and lift reduction of a 3D bluff-body using active vortex generators. *Experiments in Fluids* **48**, 771–789.

Ashpis, D. E., Laun, M. C. & Griebeler, E. L. 2012 Progress toward accurate measurements of power consumptions of DBD plasma actuators. *AIAA Paper* p. 823.

Barlow, J. B., Rae, W. H. & Pope, A. 1999 *Low-speed wind tunnel testing*. New York: John Wiley & Sons.

Barros, D., Borée, J., Noack, B. R., Spohn, A. & Ruiz, T. 2016 Bluff body drag manipulation using pulsed jets and Coanda effect. *Journal of Fluid Mechanics* **805**, 422–459.

Bayraktar, I., Landman, D. & Baysal, O. 2001 Experimental and computational investigation of Ahmed body for ground vehicle aerodynamics. *SAE Technical Paper* **01**, 2742.

Beaudoin, J. F. & Aider, J. L. 2008 Drag and lift reduction of 3D bluff-body using flaps. *Experiments in Fluids* **44**, 491–501.

Beaudoin, J. F., Cadot, O., Aider, J. L. & Wesfreid, J. E. 2006 Drag reduction of a bluff body using adaptive control methods. *Physics of Fluids* **18**, 085107.

Bechert, D. W., Bruse, M., Hage, W. & Meyer, R. 1997 Biological surfaces and their technological application—laboratory and flight experiments on drag reduction and separation control. *AIAA Paper* p. 1960.

Bellman, M., Agarwal, R., Naber, J. & Chusak, L. 2010 Reducing energy consumption of ground vehicles by active flow control. *ASME Paper* p. 90363.

Benard, N. & Moreau, E. 2014 Electrical and mechanical characteristics of surface AC dielectric barrier discharge plasma actuators applied to airflow control. *Experiments in Fluids* **55**, 1846.

Boucinha, V., Weber, R. & Kourta, A. 2011 Drag reduction of a 3D bluff body using plasma actuators. *International Journal of Aerodynamics* **1**, 262–281.

Choi, H., Jeon, W. & Kim, J. 2008 Control of flow over a bluff body. *Annual Review of Fluid Mechanics* **40**, 113–139.

Choi, H., Lee, J. & Park, H. 2014 Aerodynamics of heavy vehicles. *Annual Review of Fluid Mechanics* **46**, 441–468.

Choi, H., Park, H., Sagong, W. & Lee, S. 2012 Biomimetic flow control based on morphological features of living creatures. *Physics of Fluids* **24**, 121302.

Choi, J., Jeon, W. & Choi, H. 2006 Mechanism of drag reduction by dimples on a sphere. *Physics of Fluids* **18**, 041702.

Conan, B., Anthoine, J. & Planquart, P. 2011 Experimental aerodynamic study of a car-type bluff body. *Experiments in Fluids* **50**, 1273–1284.

Corke, T. C., Enloe, C. L. & Wilkinson, S. P. 2010 Dielectric barrier discharge plasma actuators for flow control. *Annual Review of Fluid Mechanics* **42**, 505–529.

Debien, A., Benard, N., David, L. & Moreau, E. 2012*a* Unsteady aspect of the electrohydrodynamic force produced by surface dielectric barrier discharge actuators. *Applied Physics Letters* **100**, 013901.

Debien, A., Benard, N. & Moreau, E. 2012*b* Dielectric barrier discharge plasma actuators for flow control. *Journal of Physics D: Applied Physics* **45**, 215201.

Fourrié, G., Keirsbulck, L., Labraga, L. & Gilliéron, P. 2011 Bluff-body drag reduction using a deflector. *Experiments in Fluids* **50**, 385–395.

Gilliéron, P. & Kourta, A. 2010 Aerodynamic drag reduction by vertical splitter plates. *Experiments in Fluids* **48**, 1–16.

Gilliéron, P. & Kourta, A. 2013 Aerodynamic drag control by pulsed jets on simplified car geometry. *Experiments in Fluids* **54**, 1457.

Hoskinson, A. R. & Hershkowitz, N. 2010 Differences between dielectric barrier discharge plasma actuators with cylindrical and rectangular exposed electrodes. *Journal of Physics D: Applied Physics* **43**, 065205.

Hucho, W. H., Janssen, L. J. & Schwarz, G. 1975 The wind tunnel's ground floor boundary layer—its interference with the flow underneath cars. *SAE Technical Paper* p. 750066.

Hucho, W. H. & Sovran, G. 1993 Aerodynamics of road vehicles. *Annual Review of Fluid Mechanics* **25**, 485–537.

Joseph, P., Amandolése, X. & Aider, J. L. 2012 Drag reduction on the 25° slant angle Ahmed reference body using pulsed jets. *Experiments in Fluids* **52**, 1169–1185.

Joussot, R., Leroy, A., Weber, R., Rabat, H., Loyer, S. & Hong, D. 2013 Plasma morphology and induced airflow characterization of a DBD actuator with serrated electrode. *Journal of Physics D: Applied Physics* **46**, 125204.

Julian, J., Harinaldi, Budiarso, Difitro, R. & Stefan, P. 2016 The effect of plasma actuator placement on drag coefficient reduction of Ahmed body as an aerodynamic model. *International Journal of Technology* **7**, 306–313.

Kernstine, K. H., Moore, C. J., Cutler, A. & Mittal, R. 2008 Initial characterization of self-activated movable flaps, "pop-up feathers". *AIAA Paper* p. 369.

Khalighi, B., Ho, J., Cooney, J., Neiswander, B., Corke, T. C. & Han, T. 2016 Aerodynamic drag reduction investigation for a simplified road vehicle using plasma flow control. *ASME Paper* p. 7927.

Kim, D., Lee, H., Yi, W. & Choi, H. 2016 A bio-inspired device for drag reduction on a three-dimensional model vehicle. *Bioinspiration & Biomimetics* **11**, 026004.

Kotsonis, M. 2015 Diagnostics for characterisation of plasma actuators. *Measurement Science and Technology* **26**, 092001.

Kourta, A. & Leclerc, C. 2013 Characterization of synthetic jet actuation with application to Ahmed body wake. *Sensors and Actuators A: Physical* **192**, 13–26.

Krajnović, S. 2014 Large eddy simulation exploration of passive flow control around an Ahmed body. *Journal of Fluids Engineering* **136**, 121103.

Liebe, W. 1979 Der Auftrieb am Tragugel: Entstehung und Zusammenbruch. *Aerokurier* **12**, 1520–1523.

Littlewood, R. P. & Passmore, M. A. 2012 Aerodynamic drag reduction of a simplified squareback vehicle using steady blowing. *Experiments in Fluids* **53**, 519–529.

Liu, Z., Zhang, M. & Wang, L. 2016 Investigation on 3D flow field induced by a plasma actuator with serrated electrode. *Science bulletin* **61**, 481–487.

Mazellier, N., Feuvrier, A. & Kourta, A. 2012 Biomimetic bluff body drag reduction by self-adaptive porous flaps. *Comptes Rendus Mécanique* **340**, 81–94.

McCallen, R., Couch, R., Hsu, J., Leonard, A., Brady, M., Ross, J., Stroms, B., Heineck, J. T., Driver, D., Bell, J., Zillizc, G., Browand, F., Hammache, M., Salari, K. & Rutledge, S. 1999 Progress in reducing aerodynamic drag for higher efficiency of heavy duty trucks (Class 7—8). *SAE Technical Paper* **01**, 2238.

Meyer, R., Hage, W., Bechert, D. W., Schatz, M., Knacke, T. & Thiele, F. 2007 Separation control by self-activated movable flaps. *AIAA Journal* **45**, 191–199.

Minguez, M., Pasquetti, R. & Serre, E. 2008 High-order large-eddy simulation of flow over the "Ahmed body" car model. *Physics of Fluids* **20**, 095101.

Pope, S. B. 2000 *Turbulent flows*. Cambridge University Press.

Pouryoussefi, S. G., Mirzaei, M. & Hajipour, M. 2015 Experimental

study of separation bubble control behind a backward-facing step using plasma actuators. *Acta Mechanica* **226**, 1153–1165.

Pujals, G., Depardon, S. & Cossu, C. 2010 Drag reduction of a 3D bluff body using coherent streamwise streaks. *Experiments in Fluids* **49**, 1085–1094.

Qi, X., Yang, L., Yan, H., Jin, Y., Hua, Y. & Ren, C. 2016 Experimental study on surface dielectric barrier discharge plasma actuator with different encapsulated electrode widths for airflow control at atmospheric pressure. *Plasma Science and Technology* **18**, 1005.

Robert Bosch GmbH 2002 *Bosch electronic automotive handbook*. Bentley Publishers.

Roth, J. R., Sherman, D. M. & Wilkinson, S. P. 1998 Boundary layer flow control with a one atmosphere uniform glow discharge surface plasma. *AIAA Paper* p. 328.

Rouméas, M., Gilliéron, P. & Kourta, A. 2009 Drag reduction by flow separation control on a car after body. *International Journal for Numerical Methods in Fluids* **60**, 1222–1240.

Roy, S., Zhao, P., DasGupta, A. & Soni, J. 2016 Dielectric barrier discharge actuator for vehicle drag reduction at highway speeds. *AIP Advances* **6**, 025322.

Schatz, M., Knacke, T., Thiele, F., Meyer, R., Hage, W. & Bechert, D. W. 2004 Separation control by self-activated movable flaps. *AIAA Paper* p. 1243.

Schlüter, J. 2010 Lift enhancement at low Reynolds numbers using self-activated movable flaps. *Journal of Aircraft* **47**, 348–351.

Shadmani, S., Nainiyan, S. M., Mirzaei, M., Ghasennasl, R. & Pouryoussefi, S. G. 2018 Experimental investigation of flow control over an Ahmed body using DBD plasma actuator. *Journal of Applied Fluid Mechanics* **11**, 1267–1276.

Tounsi, N., Mestiri, R., Keirsbulck, L., Oualli, H., Hanchi, S. &

Aloui, F. 2016 Experimental study of flow control on bluff body using piezoelectric actuators. *Journal of Applied Fluid Mechanics* **9**, 827–838.

Vernet, J. A., Örlü, R., Söderblom, D., Elofsson, P. & Alfredsson, P. H. 2018 Plasma streamwise vortex generators for flow separation control on trucks. *Flow, Turbulence and Combustion* **100**, 1101–1109.

Wang, C. H. & Schlüter, J. 2012 Stall control with feathers: Self-activated flaps on finite wings at low reynolds numbers. *Comptes Rendus Mécanique* **340**, 57–66.

Wang, L., Wong, C. W., Lu, Z., Wu, Z. & Zhou, Y. 2017 Novel sawtooth dielectric barrier discharge plasma actuator for flow separation control. *AIAA Journal* **55**, 1405–1416.

Zhang, B. F., Liu, K., Zhou, Y., To, S. & Tu, J. Y. 2018 Active drag reduction of a high-drag Ahmed body based on steady blowing. *Journal of Fluid Mechanics* **856**, 351–396.

3차원 자동차 모델의 항력 감소에 관한 실험적 연구: 수동적 및 능동적 유동제어

서울대학교 대학원
기계항공공학부
김 동 리

요 약

지상 운송체의 공기저항력을 줄이는 것은 관련 학계 및 산업계의 주요한 사안 중 하나였다. 그러므로, 지금까지 수동적 및 능동적 유동제어 장치를 이용하여 자동차 모델의 항력을 감소시키는 연구가 많이 이루어졌다. 기존 연구들에 사용된 유동제어장치들이 좋은 성능들을 보여주었지만, 간과할 수 없는 한계점들도 지니고 있다. 수동적 유동제어장치는 필연적으로 모델 표면에 고정된 부가장치를 설치해야 하거나 모델 표면을 변형시켜야 하며, 다양한 속도에 대해 성능이 적절하게 발휘되지 못할 수 있다. 반면에, 주로 분출/흡입 장치를 응용하는 능동적 유동제어장치는 보통 외부의 유체 흡입구/배출구가 필요하며, 심지어 다소 복잡한 구동장치가 필요하므로 실제 적용이 쉽지 않을 수 있다. 따라서, 본 논문에서는 대체 수동적 및 능동적 유동제어장치로써 automatic moving deflector와 유전장벽방전 플라즈마 액추에이터를 각각 제1장, 제2장에 제안하였다.

제1장에서, 우리는 아메드 차체의 항력 감소를 위해서 자연에서 영감을 얻은 장치가 도입하였다. AMD(automatic moving deflector)로 명명된 이 장치는 새 날개의 윗겹 깃털의 움직임에서 영감을 받아 제작되었다: 다시 말하면, 높은 받음각에서 새 날개의 부압면에 큰 유동박리가 발생할 때 윗겹 깃털이 갑자기 올라가서 착지할 때 양력을 높여준다. AMD는 아메드 차체의

뒤 경사면에 적용되어 그곳에 발생하는 유동박리를 제어한다. 경사각은 아메드 차체의 항력계수가 가장 큰 25°로 설정하였다. 풍동실험이 아메드 차체의 높이(H) 및 자유유동 속도(U_∞)를 기준으로 한 레이놀즈수 $Re_H = 1.0\times10^5$ – 3.8×10^5에서 수행되었다. 아메드 차체의 항력 측정을 통해 다양한 크기와 재질의 AMD가 시험 되었으며, 최대 19%의 항력 감소율을 보였다. 속도 및 표면압력 측정을 통해 경사면과 AMD 사이의 얇은 틈의 압력이 AMD 윗면의 압력보다 훨씬 높아질 때 AMD가 갑자기 들려 올라가기 시작한다는 것을 보였다. 우리는 또한 AMD가 작동하기 시작하는 임계 자유유동 유속을 예측하는 실험식을 유도하였다. 마지막으로, AMD에 의한 항력 감소는 주로 유동박리 지연과 경사면 양옆 가장자리에서 발생하는 유동방향 와류의 세기 억제에 따른 경사면의 압력 회복에 의한 것임을 보였다.

제2장에서, 우리는 자유유동 속도 $U_\infty = 10 - 20$ m/s에서 아메드 차체의 항력 감소를 위해서 와이어-플레이트 및 톱니형 유전장벽방전 플라즈마 액추에이터를 적용하였다. 와이어-플레이트 액추에이터의 경우, 노출전극이 지름 11 μm의 가는 와이어로 제작된 액추에이터가 아메드 차체의 경사면 앞쪽 모서리에 설치되었으며, 그것의 모델너비 방향 길이와 인가전압을 변화시켰다. 액추에이터에 의한 평균 유도 속도는 인가전압이 9 $\mathrm{kV_{p-p}}$에서 최대 4.2 m/s까지 측정되었다. 액추에이터의 작동에 의해서, 항력이 $U_\infty = 10$ m/s에서 최대 10% 감소하였으며, 효율은 액추에이터의 모델너비 방향 길이에 따라서 최대 0.1 – 0.12이다. 본 액추에이터에 의한 항력 감소 및 효율은 종래의 플레이트-플레이트 유전장벽방전 플라즈마 액추에이터의 항력 감소 및 효율보다 높다. 표면압력 측정 및 입자영상유속계를 통해 경사면 위의 유동은 액추에이터의 모델너비 방향 길이에 의해 크게 영향을 받으며, 액추에이터에 의해 유도된 유동 방향 운동량은 경사면 앞쪽 모서리에서 발생하는 유동박리를 억제하고 경사면 및 수직면의 압력을 회복시켜 결과적으로 항력 감소로 이어진다는 것을 보였다. 게다가, 톱니형 노출 전극을 사용하면 $U_\infty = 20$ m/s에서 항력 감소율과 효율이 각각 최대 8.2%, 0.56까지 추가로

향상된다는 것을 보였다. 반면, 같은 U_∞에서 선형 와이어-플레이트 액추에이터에 의한 항력 감소율과 효율은 각각 최대 2.7%, 0.1이다. 톱니형 노출 전극을 사용한 플라즈마 액추에이터의 작동에 의해서, 경사면 위에 형성되는 전단층의 발달이 촉진되며 이는 경계층 내부의 혼합을 증대시킨다. 그 결과, 액추에이터에 의해 유도된 운동량이 박리된 경계층 내부에 효과적으로 공급되어 높은 U_∞에도 불구하고 경사면 앞쪽 모서리에서 발생하는 유동박리가 크게 억제되었다.

마지막으로, 제3장에서, 우리는 수동적(AMD) 및 능동적(와이어-플레이트 플라즈마 액추에이터) 유동제어장치에 의한 효과를 요약하였고 그 항력 감소 원리에 대한 비교분석을 제시하였다. 두 장치는 모두 경사면 위의 부박리기포의 형성을 억제하여 그곳의 압력을 크게 회복시킨다. 하지만, 각 장치에 의해서 주 박리기포의 크기, 강도, 위치는 크게 달라지며, 그로 인해 각 장치에 의한 수직면의 압력 변화가 다르게 나타난다. AMD는 유동방향 와류의 세기를 억제하는 반면 플라즈마 액추에이터는 유동방향 와류에 영향을 거의 끼치지 못한다. 결과적으로, AMD의 경우 경사면의 압력 회복이 단독으로 항력 감소에 기여하며, 플라즈마 액추에이터의 경우 경사면과 수직면의 압력 회복이 모두 항력 감소에 기여한다.

주요어: 자동차 모델, 유동박리, 수동적 유동제어, 능동적 유동제어, 압력 회복, 항력 감소

학 번: 2013-23829